Escola de Camins
Escola Tècnica Superior d'Enginyeria de Camins, Canals i Ports
UPC BARCELONATECH

GEOMETRIC COMPENSATION FOR ADDITIVE MANUFACTURING

MASTER FINAL THESIS

Final Thesis developed by:
Kay, Rodi

Directed by:
Chiumenti, Michele
Caicedo, Manuel

Master in:
STRUCTURAL AND CONSTRUCTION ENGINEERING

Barcelona, 2023

Department of Civil and Environmental Engineering

Acknowledgement

I must first and foremost thank my supervisors. To Professor Michele Chiumenti and Manuel Caicedo for their devoted participation in every step of the process, for reviewing my development, and for their cosmic patience. To Mehdi Slimani, for his support, unwavering interest, and readiness to assist in times of need. Lastly, I would like to express my eternal gratitude to my loving and supportive family and girlfriend by describing the significance of their care and support for me. To my parents for their steadfast care, presence, and for serving as role models. For my girlfriend, Mirna, for being there for me, for the travels between Turin and Barcelona, for the companionship, and for the love. I would also like to congratulate everyone who taught me and helped me become the person I am today.

Abstract

During the process of Additive Manufacturing (AM), the temperature gradients are substantial and transient, resulting in irreversible residual stresses and plastic deformation that have a negative effect on the material's strength, fatigue resistance, ductility, and geometrical tolerance. These variants may not meet the necessary requirements. While various strategies, such as varying the dwell time, altering the scanning pattern, and implementing pre-heating, have been studied and successfully implemented to reduce residual stresses and distortions in AM, methods that concentrate on modifying the geometrical parameters of the structure prior to printing require additional study.

The current state of the art in this field focuses primarily on modifying the mesh of STereoLithography (STL) files to compensate for geometrical variations. Nevertheless, the current work presents an algorithm that modifies the scanning strategy in the numerical control language used for AM, in this case GCode, allowing the designer to modify the scanning strategy without having to modify the mesh and then use a slicer to generate a new GCode. This dissertation's displacement field is derived from a three-dimensional coupled Thermal-Mechanical (TM) model with a visco-plastic-elasto-plastic framework, and the employed models are industrial components such as gears, compressors, and impellers.

The results of this study indicate that the method of modifying mesh nodes produced superior results when compared to the algorithm for distortion compensation for industrial components. In particular, the algorithm was only able to reduce distortions for the same component by 30%, whereas the mesh modification method was able to reduce distortions for an impeller by 50%. This demonstrates the effectiveness of the mesh modification method in enhancing the geometrical tolerance and minimizing distortions in industrial components, making it a valuable instrument for enhancing the performance of these components.

Keywords: Additive Manufacturing, Geometrical Code, Distortion Compensation, Thermal-Mechanical Modeling, Geometrical Compensation

Acronyms

AM Additive Manufacturing.

AMR Adaptive Mesh Refinement.

CAD Computer-Aided Design.

CLI Command-Line Interface.

DED Direct Energy Deposition.

DOF Degree of Freedom.

FFD Free-Form Deformation.

HAZ Heat Affected Zone.

LPBF Laser Powder Bed Fusion.

STL STereoLithography.

TM Thermal-Mechanical.

Nomenclature

Majuscule Greek Symbols

$\Phi(\mathbf{s}, q_{\mathrm{h}}, T)$ J2-yield-surface

∇ Divergence operator

Ω_{a}^{n} Domain of previously activated hatches

$\Omega_{\mathrm{a}}^{n+1}$ Domain of activated hatches

Majuscule Roman Symbols

$\dot{D}_{\mathrm{mech}}$ Thermal-Mechanical dissipation

$\dot{H}$ Enthalpy rate

$\dot{Q}$ Heat source

K Bulk modulus

C Heat capacity

G Shear modulus

L latent heat released during the phase-change process

$R_{\mathrm{q_h,T}}$ Yield-surface radius

S_{σ} Neumann boundary (tractions)

S_{q} Neumann boundary (heat flux)

S_{T} Dirichlet boundary(temperature)

S_{u} Dirichlet boundary (displacement)

T Temperature

T_{env}^{4} Fourth power of thermodynamic temperature in the environment

T_{clamp} Temperature in substrate

T_{env} Temperature in environment

T_{L} Temperature at liqudius

T_{sub} Temperature in substrate

T_{S} Temperature at solidius

V Open and bounded domain

Minuscule Greek Symbols

χ	Isotropic strain-hardening variable
$\delta\mathbf{v}$	Variations of displacements
δp	Variations of pressure
$\dot{\gamma}$	Visco-plastic multiplier
$\dot{\lambda}$	Visco-plastic multiplier
$\eta(\dot{\gamma})$	Viscous overstress
$\boldsymbol{\sigma}$	Cauchy stress tensor
ρ	Density
ρ_0	Density at liquid phase
ρ_0	Density at solid phase
ρ_0	Density at the initial temperature
σ_{h}	Hydrostatic stress
σ_{eq}	Equivalent stress yields
σ_{rad}	Stefan-Boltzmann constant
$\sigma_{\mathrm{y}}(T)$	Initial yield stress
ε	Strain
ε^e	Elastic strain tensor
ε^p	Plastic strain tensor
ε^{vp}	Visco-plastic strain tensor
$\varepsilon_{\mathrm{rad}}$	Surface emissity

Minuscule Roman Symbols

$\mathbf{s}$	Deviatoric stress
$\mathbf{n}$	Normal to the yield surface
$\mathbf{q}$	Heat flux
p	Hydrostatic stress
$\overline{q}$	Prescribed heat flux

$\mathbf{b}$	Body forces
d_0	Interplanar spacing
e^T	Thermal deformation
e^{cool}	Thermal dilation
e^{pc}	thermal shrinkage
f	Residual force
f_L	Fraction of liquid
h	Heat transfer coefficient
h_cond	Heat transfer coefficient by conduction
l_i	hatch length
p	Pressure
$q_{\chi,\mathrm{T}}$	Stress-like variable that controls the isotropic hardening phenomena
q_cond	Heat flux by to conduction
q_conv	Heat flux by convection
q_rad	Heat flux by to radiation
t_i	Time for a given activated hatch length
u	Displacement

Number Sets

$\mathbb{R}^3$	Three-dimensional Euclidean space

UNIVERSITAT POLITÈCNICA DE CATALUNYA BARCELONATECH

Table of Contents

UNIVERSITAT POLITÈCNICA DE CATALUNYA BARCELONATECH

List of Figures

1 Introduction

1.1 Motivation

Additive Manufacturing (AM), or customarily "3D-printing", is a recent phenomenon that was revolutionized four decades ago and is rapidly increasing in popularity. It is used in a vast array of industries, including aerospace, medicine, and the energy sector. Typically, the application of AM is determined by attention to detail and precision. For instance, modern jet engines and landing gear made from titanium alloys are utilized in spacecraft and air shuttles. With such a high level of responsibility comes the need for precise and consistent manufacturing for performance, not only for the mechanical properties of high strength, significant ductility, and fatigue resistance, but also for fabrication tolerances in terms of geometry. However, titanium alloys are produced at high temperatures, which can cause the final product to be deformed and therefore not meet the fabrication tolerance required for service [1].

Consequently, enhancing manufacturing performance is of the utmost importance. Changing diverse parameters, including temperature gradients and backspeed, can lead to adequate production. Nonetheless, titanium alloys are costly, both for production and manufacturing, and iterations are therefore discouraged in *in situ*. Finding the precise code and parameters for numerical manufacturing has a number of advantages, including significantly cheaper processes, the absence of material usage, and free iterations.

It is essential to comprehend the root causes of warpages and deviations in order to develop effective solutions. The numerical precision of simulations used to predict these distortions must be as reliable as possible. Several finite element analysis techniques can be used to address this issue. However, a three-dimensional Thermal-Mechanical (TM) analysis is a widely-used method in AM for Direct Energy Deposition (DED) and Laser Powder Bed Fusion (LPBF). One of the disadvantages of this high-fidelity method is that it necessitates a substantial amount of computational time, which can be impractical for industrial applications. Utilizing Adaptive Mesh Refinement (AMR) techniques is one potential solution to this problem. During transient analysis, this method refines the mesh only in the regions of the geometry that are within the Heat Affected Zone (HAZ), while the remaining geometry remains relatively coarse. This can significantly reduce the computational time required, making it more efficient for industrial applications.

As a result, finding an appropriate TM solution to address or counteract the effects of AM distortions is crucial. Presently, the majority of research and development efforts in this area have centered on utilizing pre-machinery solutions, such as heating the substrate, adjusting temperature gradients, and implementing cooling strategies, to alleviate the problem. Conversely, post-machinery mitigation techniques are relatively under-explored. This thesis will therefore concentrate on investigating and developing methods for compensating for geometric distortion.

1.2 Objective

The primary objective of this dissertation is to significantly reduce or eliminate the unwanted distortions that occur during the AM process of LPBF for the alloy Ti-6Al-4V. Despite the use of various mitigation strategies, warpage can still exceed the fabrication tolerance, making the final component unsuitable for use. The ultimate goal is to develop a method that can reduce the distortions to an acceptable level, ensuring that the final component is in line with the nominal geometry, with minimal or null distortions

1.3 Outline

The dissertation begins with a thorough review of the current state of the art in the field of AM and TM modeling. The literature review will cover various technologies utilized in metal 3D printing, including the advantages and limitations of each. Additionally, it will provide an in-depth examination of the challenges associated with coupled TM modeling and the numerical control language for AM, as well as the methods for automatic mesh generation. The literature review will also delve into various mitigation strategies, with a specific focus on geometric-distortion compensation strategies, examining their effectiveness and limitations. This comprehensive literature review will provide a solid foundation for the research presented in the remainder of the dissertation.

The methodology employed in this dissertation involves the use of a three-dimensional coupled TM model that incorporates a visco-plastic-elasto-plastic framework. The governing laws, boundary conditions, and material behavior that will be used to determine the displacement field for the industrial components will be presented in detail. This displacement field will then be used to demonstrate the methodology of geometric compensation. The results of this study will be presented and discussed in detail, providing insights into the effectiveness of the methodology and the potential improvements that can be achieved. Furthermore, the discussion will also include the limitations and potential areas of future research. Overall, this dissertation aims to provide a comprehensive analysis of geometric compensation in industrial components, making it a valuable resource for engineers and researchers in the field of AM.

2 State of the art

2.1 Additive Manufacturing

AM for metals truly began in the 1980s with the revolution of "3D printing" in general, when the DED technique was developed: The process consists of utilizing a deposition material in powder or wire form, which is melted onto a substrate material with a laser or electron beam, and it is a machinery process using computer-aided motion; consequently, it is more precise and prevalent than for instance multi-pass welding [2].

Later industrialization of AM for metals formed with LPBF machines, which use an extremely small heat source to melt a fusion powder on a substrate and, after melting each layer, the platform descends with the height of the solidified powder, *Figure 1* depicts the LPBF melting process for a layer, which is subsequently covered with new powder.

LPBF processes are less demanding to setup for the engineer compared to DED processes. Because for DED the code usually has to be manually set up for the controller In contrast, the LPBF utilizes an STereoLithography (STL) or Computer-Aided Design (CAD) file in conjunction with Slicer software to generate a machine-specific file. Thus, the quality is superior compared to DED when manufacturing high-resolution components [2]. However, some machines has evolved the technology of instead of manually producing a code for the controller, or slicing the STL, the engineer has the option to send the CAD file to the machine, and from there, let the machine produce a code.

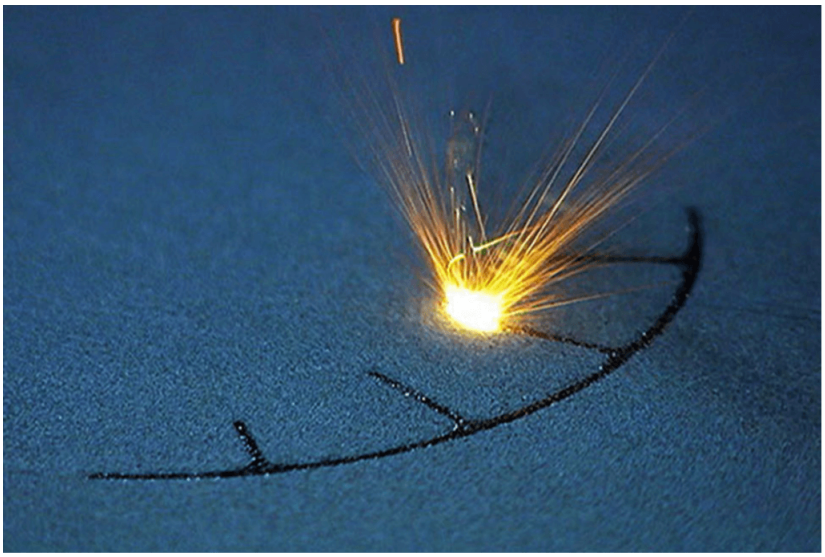

Figure 1: Heat source melting a powder bed according to the AM technique LPBF [3]

2.1.1 Direct Energy Deposition

As stated previously, DED procedures utilize computer-assisted movement, most frequently a GCode, which is a numerical control programming language that describes machine motion. Analogized to the LPBF, the DED does not melt already placed powder on the melt pool but injects the material on the substrate instead. Therefore, the necessary components for DED processes are as depicted in *Figure 2* , a laser beam injecting the powder, that comes from a powder feed. This laser beam can either be high powered laser or an electron beam. While a laser beam possesses a significant amount of heat source power and can be utilized in either a closed or open chamber, an inert gas is required to prevent the contamination of the component by gases. In contrast, an electron beam must operate in a vacuum and its efficiency is significantly greater than that of a laser: between

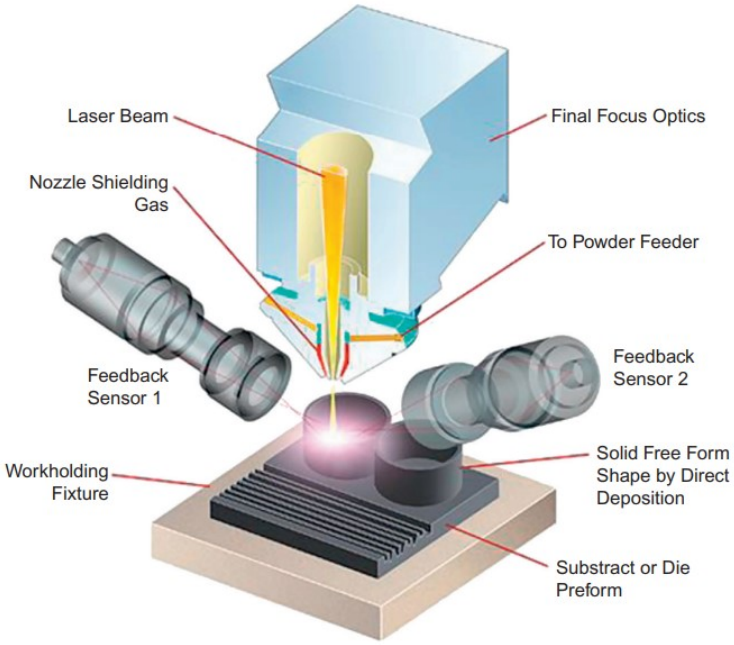

Figure 2: DED technology [5]

90 percent for an electron beam versus 30 to 50 percent for a laser. Feedback sensors and final focus optics are used for precision [4].

This process involves layer-by-layer deposition until the component is finished, and as previously stated succinctly, residual stresses between each layer are anticipated due to varying temperature gradients; this is one of the most significant disadvantages of DED processes.

As depicted in *Figure 2*, the DED method begins with the placement of a substrate, which is typically composed of the same material as the manufactured component. This substrate serves as the base upon which the material is deposited.

To create a controlled environment, the machine chamber is then sealed off with an inert gas, such as argon or nitrogen. This is essential for reactive metals such as Ti-6Al-4V, as it prevents oxidation and other reactions that could compromise the final product's integrity. For relatively less reactive materials, such as steel, it may not be necessary to use an inert gas chamber, and local shielding can be used instead.

Deposition can occur when the material is deposited onto the substrate through a nozzle or metal wire, depending on whether the DED process employs a laser or electron beam. This process is capable of producing high-quality components with a high level of precision, as it allows for the precise control of the energy input and the shape of the deposited material [6].

2.1.2 Laser Powder Bed Fusion

LPBF processes are similar to DED, with the layer-by-layer deposition, and a heat source controlled by a numerical control commands for AM. However, the difference is that the powder for LPBF is already placed, whereas DED injects the material. This will allow the heat source to be small compared to the DED laser beam. Thus, the geometry done by LPBF processes is much finer, and detailed geometrical components are usually preferred for this process than DED, *Figure 3* shows a schematic demonstration of the whole process

in more detail. Nonetheless, residual stresses and distortions are still present in this system as well.

The powder has to be recoated every layer by a recoater, where the recoater can be made of either metal, polymer, or a roller. The powder depositor will recoat the whole layer after the melted powder is cooled down. However, if the distortions upwards of the component are large enough to surpass the beginning height of the succeeding, and the recoater starts to deposit powder the blade of the recoater can suffer damage if the blade is metallic. Whereas, for polymer and roller systems, the effectiveness of the process is decreased. Hence, the distortions in LPBF procedures are not solely regarded for the built component, but the effectiveness and condition of the machinery.

Figure 3 shows a schematic demonstration of the whole process in more detail.

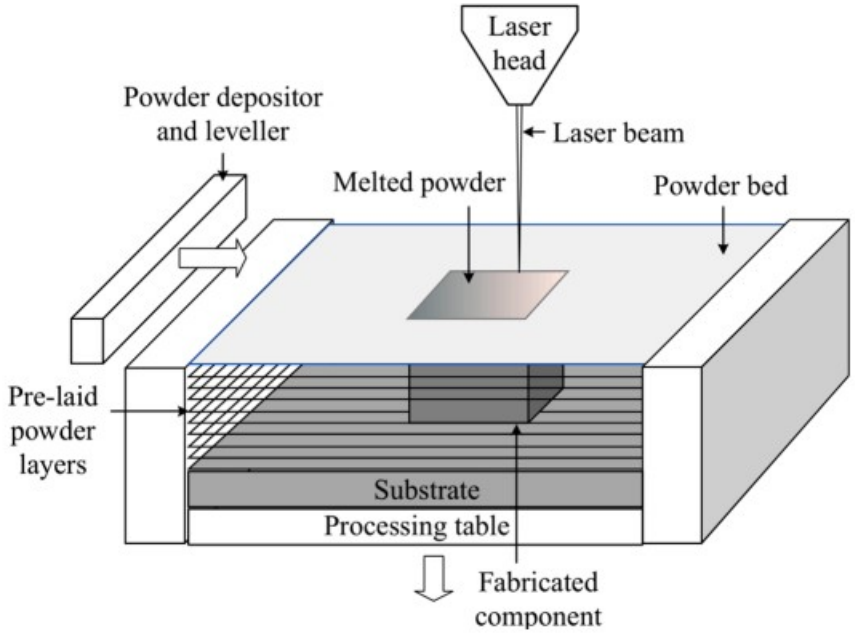

Figure 3: LPBF technology with a laser beam melting the powder on its bed [7]

2.2 Numerical Control Language for Additive Manufacturing

The manufacturing machine, as illustrated in *Figure 2*, requires precise control commands to properly execute the manufacturing process. These commands include parameters such as power input, geometrical description, and intermediate pauses between printing commands. Before the machine can be used, the designer must go through several stages of preparation. This includes creating a CAD model, converting it to an STL file, and using a software called a Slicer (as shown in Figure 5) to generate the GCode. The Slicer takes the STL file or 3D model and converts it into a numerical control language containing the necessary printing instructions. Additionally, the Slicer allows for the modification of parameters such as printing speed and dwell time to further optimize the manufacturing process.

In addition to GCodes there are other control languages, one popular is Command-Line Interface. Which is structured to describe the geometry. However, other parameters must be included separately, which is a disadvantage in comparison to GCodes. For instance, *6* displays a different feeding rate for the entire component; this would not be possible with a CLI code alone, as the entire component would have the same parameter regardless.

The advantage of using GCode as the machine's control language is that it allows for the specification of variables other than those that can only be expressed geometrically, such as speed, material extrusion, power input, and interim cooling pauses. Each command has a unique definition; the first is G0/G1, which denotes linear motion. G1 is a linear motion with a feeding rate, as opposed to G0, which describes a cooling linear motion without extruding material. Since X, Y, and Z Cartesian coordinates are adhered to throughout each command, these two commands are the primary ones for describing the geometry of the components [8]. The program will be able to discern when to change coordinates and when not to as a result, which is another benefit. As long as the coordinates are unchanged, they will remain unchanged until a new parameter is specified.

Additionally, the F command can be used to describe the speed. A sample of GCodes commands used to describe the movement of an impeller can be found in *Figure 4*. The sample also makes use of command codes E and S, which stand for extrusion and pause time in seconds, respectively. These codes are extremely advantageous when used in conjunction with G108 and F, which control power and speed, because they can be used to reduce residual stresses and distortions by adjusting temperature gradients [9]. *Table 1* demonstrates different GCode commands and their respective descriptions.

Table 1: GCode commands

Code	Description
G0	Linear cooling interpolation
G1	Linear interpolation with a feed
G4	Dwell
F	Feedrate
E	Extrusion of material
S	Dwell time in seconds
X	X-axis of machine
Y	Y-axis of machine
Z	Z-axis of machine

Figure 5 illustrates different color schemes done by the GCode showing different line types. However, it is also possible to visually depict the various parameters and their values described in the GCode.*Figure 6* is an illustration of different feeding speeds on different surfaces of a component, with blue representing a relatively slower speed than orange.

2.3 Finite Element Modeling

To accurately determine the distortion produced under the AM a FE discrete simulation has to be computed. There are numerous approaches to efficiently compute the stresses and strains, and predict warpage, however, the inherent strain method and TM modeling are the most promising. The TM model with a layer-by-layer approach and AM has the advantage of being able to efficiently calculate distortions and residual stresses without requiring an extensive FE analysis, when regarding the computational time. One of the most realistic printing strategies for AM is hatch-by-hatch, which requires one computational time step per unit of printed material length, this strategy is considered to be the high-fidelity one, particularly when the longitude of all the hatches are considerable small compared to the representative size of the printing piece. In order to speed up the printing process, there are some alternatives to include than one hatch per time step; one of them is the

```
G1 F2400 X139.279 Y120.087 E930.85274
M204 S5000
M205 X30 Y30
G0 F15000 X139.037 Y119.834
M204 S500
M205 X5 Y5
G1 F2400 X139.427 Y119.444 E930.86787
M204 S5000
M205 X30 Y30
G0 F15000 X139.185 Y119.191
M204 S500
M205 X5 Y5
G1 F2400 X138.795 Y119.58 E930.88298
M204 S5000
M205 X30 Y30
G0 F15000 X138.554 Y119.327
M204 S500
```

Figure 4: Example of a GCode

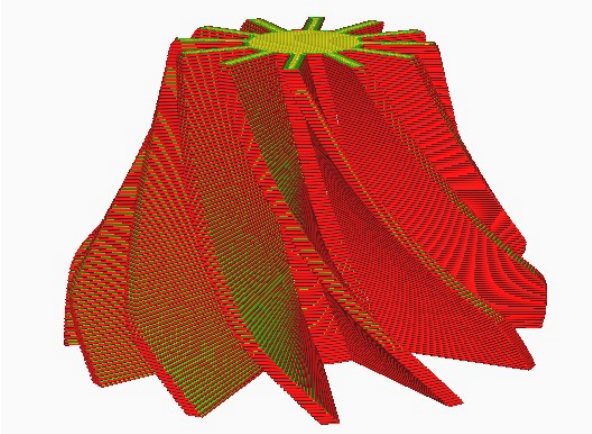

Figure 5: The color scheme in Ultimaker Cura (Slicer) describes different line types and commands depending on the color

layer-by-layer strategy, which consists of an entire or multiple layers for each time step. Thus, it is less accurate than hatch-by-hatch but requires significantly less computational time.

Computational time is of the utmost importance, and a large number of iterations can incur substantial costs. AMR, which refines the mesh around the HAZ during heating while leaving the remaining geometry coarse, is one method for mitigating this issue. Since temperature is non-linear in space, time, and position-dependent, it affects, the plasticity, and viscosity. As a result of the alloy's exposure to significant temperature gradients and multiple phase transformations, the mechanical properties will behave differently depending on temperature. It undergoes non-linear phases and has predictable properties across a range of temperatures. However, the non-linear behavior often occurs at extreme temperatures [2].

2.4 FE Mesh Generation

This section provides a brief methodology of octree meshing and automatic mesh generation with cube boxes, which is required for this dissertation when solely a GCode is used to compute a simulation. The simulation of the heat input becomes more challenging when

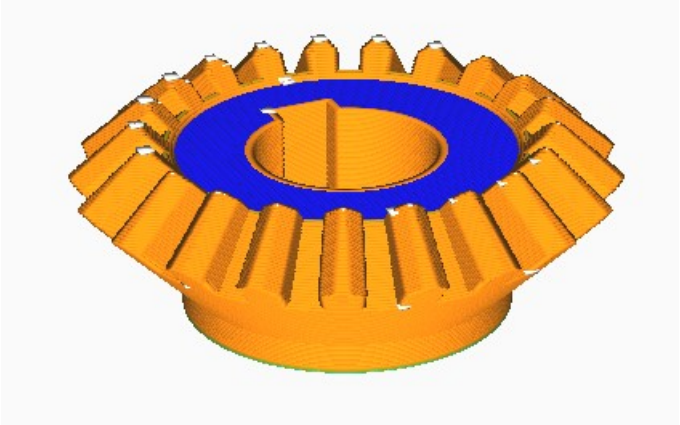

Figure 6: The color scheme describes different feeding rates

dealing with LPBF processes, this is because of the jump of scales between the HAZ and the representative size of the printed piece.

2.4.1 Octree meshing

The FE mesh is generated using an octree structure, a tree-like structure in which each parent node has exactly eight offspring. This hierarchical structure allows for a high degree of control over the level of refinement, with each additional level resulting in the uniform division of the initial element into eight smaller elements. As seen in *Figure 7*, the octree algorithm begins with a single element, which is then refined according to the desired level of precision. This process is particularly useful for generating meshes for the analysis of high-complexity structures, such as those found in the HAZ.

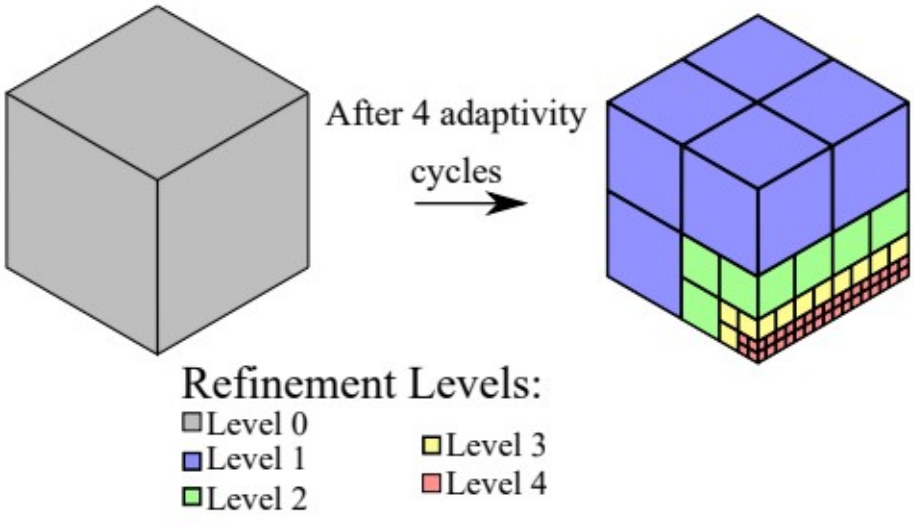

Figure 7: Adaptive mesh after a refinement level of 4 at the HTZ [9]

2.4.2 Automatic meshing

Adaptive Mesh Refinement (AMR) is a powerful tool that automatically meshes the path during the manufacturing process. It uses the path of the GCode or CLI code to segment the path into individual hatches or layers, and then uses a specified time interval to calculate the number of time steps. The key variable in this process is the deposition length increment per time step, denoted by Δl. This value is used to determine which

hatches will be activated during a given time step. To accomplish this, the HAZ adds all of the non-activated hatches until they reaches Δl . This creates a highly efficient and accurate mesh generation system that can be easily integrated into any manufacturing process.

During the simulation, the activated hatches are those within the HAZ. The time can then be defined for each path length increment such that the accumulated time from all previous steps is subtracted from the current time step. *Figure 8* illustrates each increment length and the corresponding time step. Observe that purple hatches are activated in the time step n+1, whereas the previously activated hatches are the green in the previous time step.

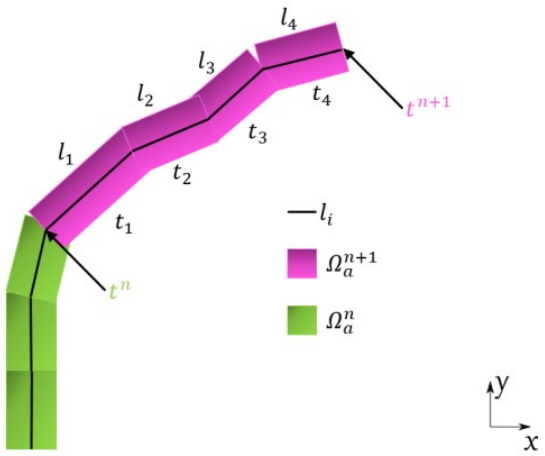

Figure 8: Depiction of activated hatches (Ω_a^{n+1}) during manufacturing, and previously deposited hatches (Ω_a^n), with the hatch length l_i and the corresponding time, t_i for each hatch length [9]

After defining the time-stepping and hatch path, the final step in the process is to define the bounding boxes. The bounding boxes are defined to identify, via collision detection algorithm, the number of FEs to be activated in the current time-step. These three-dimensional bounding boxes are dependent on several factors, including the layer thickness, melt-pool height, heat source penetration, and melt-pool width. The mesh is then generated by activating every element that is within the bounding box during the manufacturing process. It is important to note that the element size is specified by the user and is dependent on the octree refinement algorithm. The user needs to make sure that the element size is small enough to capture the details of the process, but not so small that it causes computational issues. Therefore, the choice of element size is a trade-off between accuracy and computational cost.

For a more detailed explanation, see [9].

2.5 Challenges with Thermal-Mechanical Modeling

Regarding the challenges of the TM model, depending on the AM technology metals, the challenges can differ. However, there are some challenges to the approach that are usually common:

- Thermal losses
- Modeling the heat input

- Integrating thermal and mechanical behavior
- Deposition of the material
- Modeling the elasto-plastic behaviour accurately

In addition to the difficulties associated with accurately determining heat losses, modeling appropriate elasto-plastic behavior, coupled TM modeling, and heat input, etc., computational time, convergence, and precision are extremely challenging for FE discrete models in general.

The inherent strain method has shown promising results for reducing the computing time significantly since the model is calculating at without using a temperature field. Since the TM model is replaced by a purely mechanical solution. The method consists of assuming a user defined inherent strain field which gathers both the thermal and the plastic strain components. However, determining these inherent strains is a problem that requires either multi-scale or local–global modelling; or empirical data taken from experiments [10].

2.5.1 Thermal Losses

The thermal losses must be reduced in order to provide an accurate value of the thermal field to the mechanical problem. This is a crucial aspect of the thermal problem. These thermal losses are measured as the difference between heat input and energy stored in the system. Since accurately describing them will affect their mechanical behavior and, consequently, the stresses and deformations of the structure, it is necessary to describe them precisely. Generally speaking, in thermal problems, convection, conduction, and radiation losses are the three main contributors [2].

Conduction

The transport of heat through a solid material by way of the movement, is one of the fundamental heat transfer mechanisms in AM. A heat source, such as a laser or an extruder, is used to introduce heat to the material during the printing process. The heat input flows by conduction through the whole printed part and the substrate.

Convection

In addition to conduction, convection is another important mechanism of heat transfer in AM. When heat is transferred from a solid surface to a moving fluid or gas, convection heat loss occurs. This can happen during the cooling process as heat is transferred from the hot printed object to the surrounding air or coolant. Several factors determine the rate of heat loss due to convection. Some of them are: the thermal properties of the material, the temperature difference between the printed object and the surrounding fluid, and the velocity of the fluid.

The fluid velocity and temperature can vary considerably based on the cooling system employed and the printing conditions, making the accurate depiction of fluid flow one of the most difficult aspects in AM process. Moreover, the geometric complexity of the printed parts and the nature of the layer-by-layer printing process may make it difficult to precisely record the temperature distribution within the printed part.

Thermal radiation

Thermal radiation is considered as the transfer of heat through electromagnetic waves without the need of a medium. During the printing process in AM, thermal radiation may occur as heat is transferred from the heating source to the material being printed. The

rate of heat transfer via thermal radiation is dependent upon the thermal properties of the material, the temperature of the heating element.

Radiation heat transfer is a complex phenomenon that depends on the emitting and absorbing surfaces, their emissivity, reflectivity, and absorptivity,

2.5.2 Heat Input

According to all AM processes, the heat input must be modeled to simulate the laser heat source, which attempts to simulate the temperature field that influences the formation of residual stresses and deformations. Given the magnitude of the heat input and the heat source's efficiency, it may be difficult to accurately replicate this in the discrete FE model.

Also, due to the minuscule size of the heat source in LPBF processes, this can be challenging.

2.5.3 Thermal and Mechanical Coupling

Due to the characteristics of AM processes, a coupled thermal and mechanical problem must be used. In this instance, the thermal gradients under the manufacturing process have a significant impact on the material's mechanical properties, which in most cases exhibit nonlinear behavior. Consequently, the effectiveness of the method is contingent on the precise computation of the temperature field; otherwise, its error will be automatically transferred to the mechanical problem.

To do so, several options for solving this coupled problem can be considered. The monolithic scheme being the most complex one due to the fact that mixing state variables may yield u-conditioned linear systems. However, some problems can be simplified by coupling them and considering two separate models, thermal and mechanical, and solving them independently in a staggered fashion.

Another simplification is a decoupled model. A decoupled TM model is predicated on the behavior being unidirectional, which means that the thermal range influences the mechanical properties, but the mechanical properties have no effect on the thermal properties of the alloy. However, this is not applicable whenever warpage distresses the system boundaries [2].

2.6 Residual stresses and distortions

Throughout the deposition, the building process will experience significant dynamic temperature gradients, as the material will first be applied to a cooler body, followed by successive layer construction. These variations within a constrained body will introduce residual stresses, that in, most cases exceed the elastic yield strength of the component and, as a result, cause plastic deformations and strains [2][6].

In addition, the alloy's phase change from liquid to solid introduces residual stresses that can be small or substantial, depending on whether the phase-change is from solid-to-liquid or the other way around. *Figure 9* depicts the change at an atomic level, where the stress can change the lattice structure, and if the deformation remains after removing an imposed stress, the residual stress will remain [1].

2.7 Distortion mitigation strategies

Overall, there are several solutions to mitigate and compensate for distortions in AM. The vast majority of published works only present a single solution, as opposed to a comprehensive design strategy to fully compensate for distortions or at least mitigate their effects to a level sufficient for fabrication tolerance using predominantly conventional methods. To date, however, it remains challenging to compensate for the causes of defects, which may include material shrinkage, machine defects, temperature history, etc.

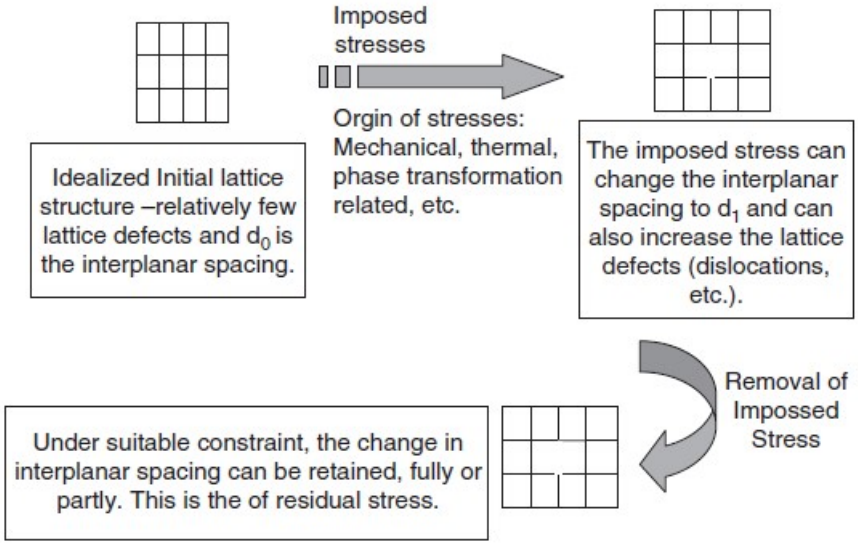

Figure 9: Stresses are exerted on an undeformed, idealised material with interplanar spacing d_0. This may result in an alteration in interplanar spacing and an increase in lattice defects. If retained in full or in part, the former is residual stress [1]

2.7.1 Geometric-distortion Compensation

The objective of geometric-distortion compensation is to modify the initial geometry in order to compensate the final product, for undesired warpage. The methodology is done by calculating the distortions (or scanning them from an already complete part) and invert the coordinates of the initial geometry, in the design stage, in order for the "wrong" geometry to distort back into the intended geometry. This methodology is depicted in *Figure 10*.

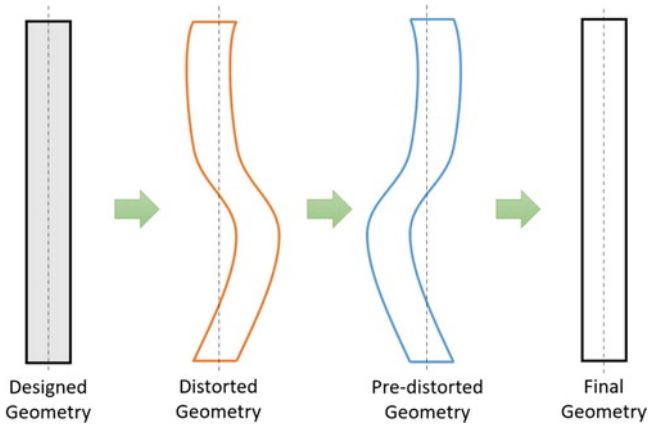

Figure 10: Concept of geometric compensation by solely changing the geometric parameters [11]

Several authors have already demonstrated numerical solutions for geometric-distortion compensation for AM, which was also tested with experiments. In [12] introduced an approach to geometric compensation. Here, the method is based solely on pure geometric compensation; consequently, only the geometric parameters are modified after computing the distortion caused by thermal gradients and material shrinkage. Once the distortions are computed, the geometry is properly modified, and if the geometrical tolerance is not sufficient, iterations must be performed until the tolerance is satisfied.

Figure 11 shows an example where the displacement is fully compensated after an iterative process. Using this strategy, the plastic deformations of the AM component were drastically reduced. Even with decreased substrate stiffness, which results in increased deformations [12].

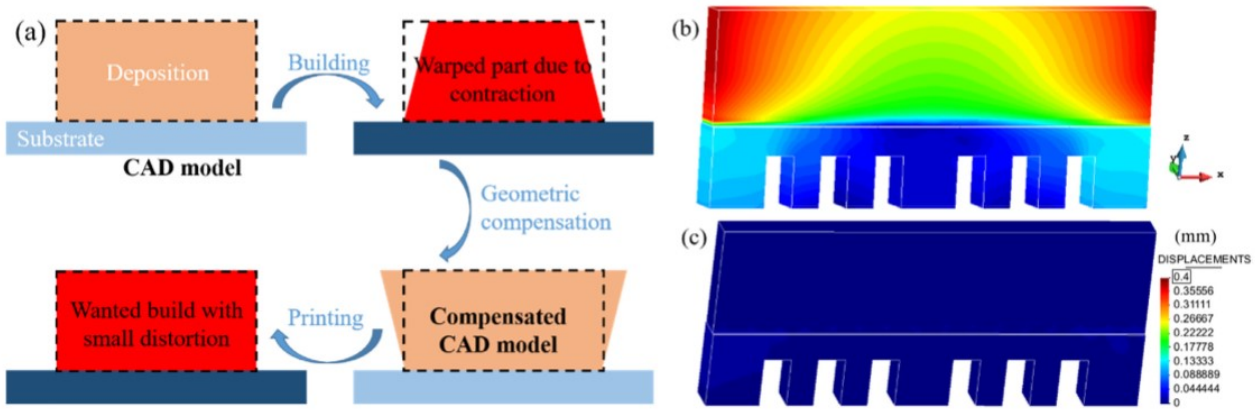

Figure 11: Geometric compensation methodology by changing the CAD model, resulted in full compensation when comparing CAD's [12]

In [13] uses a two-dimensional TM model to simulate the distortions. In this case, the dependent material is a Ti-6AI-4V. In this experiment, once the distortion of the whole piece has been obtained the initial gentry is modified to compensate for it. This exponent is based on a cylindrical geometry where a local buckling due to the printing process is detected The distortions exceed 10mm. However, after compensating the distortions by using a pre-distorted CAD file, the distortions were significantly reduced. In consequence, no buckling phenomena occur in the printed piece. Thus, iterations were not necessary since the results were sufficient.

The use of 3D optical scanning has also been recommended as a method for minimizing distortion in AM. This method involves first scanning the entire component using a 3D scanner to obtain the coordinates to create a mesh. In a second step cleaning the surface mesh is cleaned in regions close to the supports (clean mesh means removing the unnecessary parts). With the refined and cleaned mesh, displacements can be calculated, and an inverse analysis by changing the geometry with the known distortions can be performed, similar to the first method using the FE discrete analysis. This method involves many more steps than the FE analysis, but it can provide a more detailed and accurate representation of the distortions that occur [14].

Comparisons between the two results suggest that both methods are compatible and have their own advantages. Whereas 3D optic scanning may not have the capacity to scan the whole surface of the components, the distortions of the inner and outer surfaces of the component are assumed to follow an equal pattern.

In [11] developed a geometrical compensation method by improving a mathematical model that calculates the distortion vectors of two aligned surface meshes; this method outperformed the methodology proposed in [15]. This new method showed greater results in sharp corners and small radii, while [15] had problems within their mathematical model. However, the strategy for mitigation is similar to some of the previous ones, the geometry set is equal to the inverse of the distorted geometry; *Figure 12* shows an example of inverting a node. The part was subjected to buckling as well, with distortions being around 400µm but after using their mathematical model, the results indicate distortions

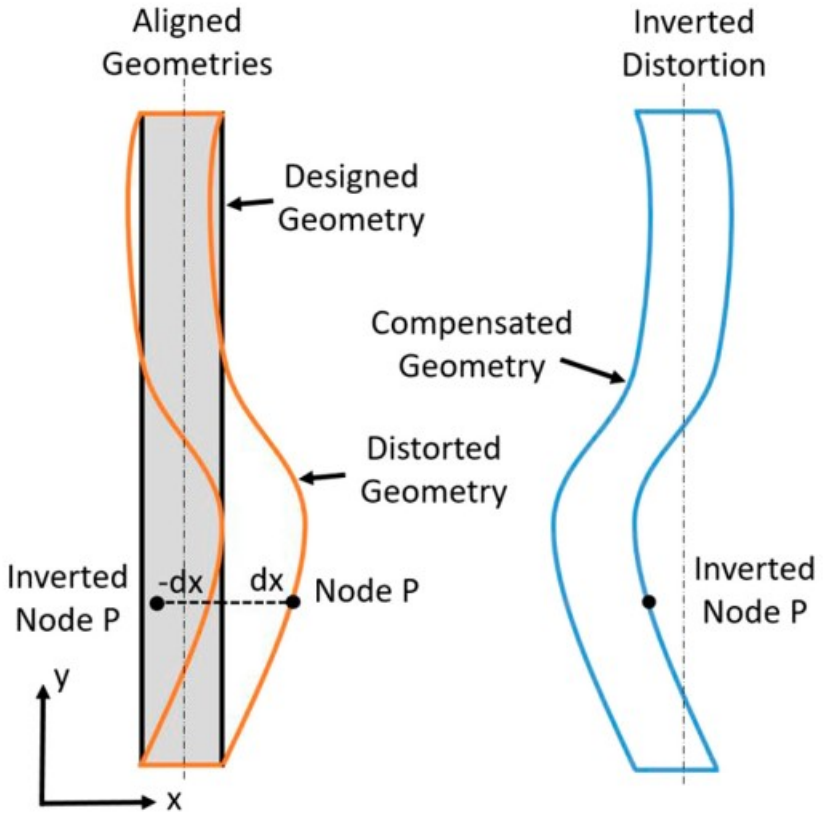

Figure 12: Distortion inversion concept [11]

around 100 µm, with is a reduction of 75%. The method is based upon using a surface mesh, that is optically scanned after manufacturing the component, whereas the mesh is defined by triangular elements with three nodes (the original mesh is defined by 3 points, as well as the distorted surface mesh). Here the mathematical model comes in; the objective of the mathematical model is to find which node of the original triangular element that is related to the distorted node of the distorted surface mesh. Relating the distorted node with the original node makes it possible to proceed with the distortion-compensation methodology.

One study, [16], offers TM for DED manufacturing with large-scale components. This is one of the few studies on DED procedures with large-scale components, as the majority of previous research relies on simplifications such as symmetrical parts or decoupled thermal models. In this study, the authors utilized a high-fidelity approach with a small decoupling by mechanically solving only every fourth iteration. According to the authors, the slight decoupling should not have had any negative effects on the final result. Additionally, with the distortion compensation strategy, a new scanning pattern can be generated by starting with the distortion-negative on the generated mesh. For the first iteration, the distortions were reduced by 65%.

In [17], a FEA was used to simulate the distortions of an impeller. With the distortions predicted by FEA, they are implemented into an STL file containing the geometry. Thereafter, a negative sign from the distortions was used on the nodes of the mesh file, which should result in the geometry distorting back to the intended geometry. The component was again manufactured using AM, after the numerical simulations with the new STL file. After manufacturing, the distortions were scanned and compared to the

initial impeller. The comparison indicates that the warpage was mitigated, comparing to the L-infinity (maximum displacement) metric, the results indicate a 50% reduction in distortions.

2.7.2 Dwell time

In AM the dwell time is considered as the time when the machine is fixed at a certain point, being a source of the distortion. In consequence, less dwell time can minimize the distortion and residual stresses. On this basis, the dwell time can be used to reduce distortion and enhance the final product's fabrication tolerance. For this particular study, the dwell time ranges from 0 to 40s, a null dwell time resulting in almost no accumulation and an increase in distortion after the initial phase. However, this was not the case for dwell times in the 20s and 40s, where distortion could increase after the initial phase. Overall, the accumulated distortion decreased by 81.7% after the first layering, but then increased after 30 minutes of layering. Similar to residual stresses, the case with null dwell time exhibited the lowest residual stress, and, the peak temperature was the highest because heat loss via convection and radiation was reduced in comparison to cases with longer dwell time, see i.e [18].

2.7.3 Free form deformation

In [19] the possibility of pre-compensation is discussed, which is the same theory as changing parameters before production, which can be done by Free-Form Deformation (FFD). This technique involves deforming a cube surrounding the component, which will consequently deform the component by deforming the cube. In other words, the deformation of the cube is transferred to the component, which causes a change in the shape of the component. The cube is deformed in such a way that it compensates for the distortions that would otherwise occur during the printing process, the component inside the cube will also be deformed to that it compensates these distortions.

It is worth noting that the deformation of the cube is not a physical deformation, it's a mathematical deformation that is coupled by using algorithms and mathematical models. The deformation of the cube is performed on a digital model of the component, see i.e [20]. The deformed model can then be used to generate the instructions for the printer (G-code) or to generate the final STL file.

However, for this technique to be successful, suitable parameters must be known beforehand. These parameters are based on warpage, and different distortions phenomena can be grouped into categories of warpage effects. Depending on the phenomena, the mathematical function used to deform the cube can differ, as well as the order, number of control points, etc.

One approach is to use experience-based pre-compensation. First, mathematical models for standard geometries are created and implemented into the software that supports FFD. FFD can be done by using a mathematical model considering graph theory, trivariate B-spline functions, or Bernstein polynomial, which can be used as a function or generalization in Bezier curves. The theory is based on controlling points and changing their position to change the overall geometry with three-dimensional parametric curves.

Second, simple parameters from the warpage effects can be determined after iterating the component and calculating the warpage, and used in the pre-compensation file by reversing the FFD control points and using a suitable amplifier to mitigate the distortions see i.e [21].

However, this approach could be undesirable in AM processes, as the data is not solely

dependent on the CAD file and is not distributed uniformly across the entire component. Control volumes can be used as an alternative to control points to implement the FFD into AM machinery. Whereas, the control volume is a volume made of 4 control points, as shown in *Figure 13* [22]. Given that FFD is applicable to both global and local solutions, this is a suitable solution for AM. Consequently, these volumes can represent different layouts with different volumes within the component, as AM can be significantly diverse within the same manufacturing process and the FFD is utilized locally.

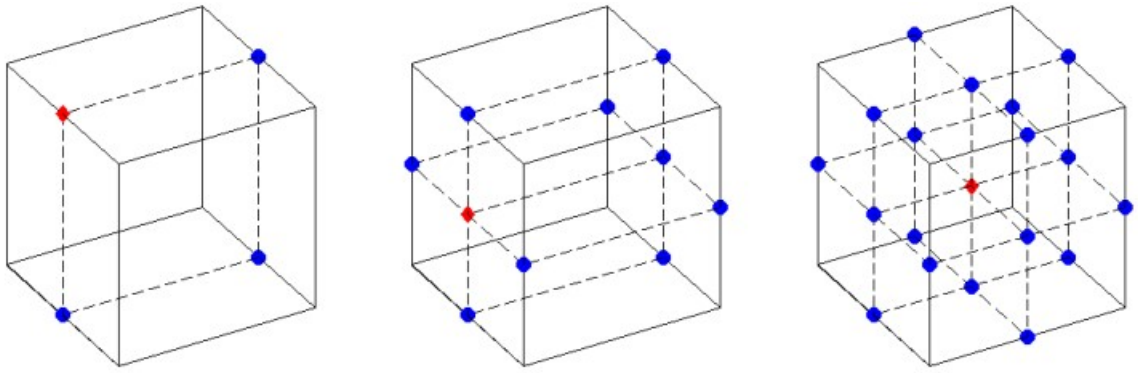

Figure 13: A number of points controlling the volume which can be used to modify it [22]

2.7.4 Pre-heating

As the construction of the alloy is now performed on a heated surface as opposed to a substrate at room temperature, it is possible to reduce the residual stresses by heating the substrate of the building chamber. However, this may be inefficient for large substrates because the entire substrate must be heated for an extended period of time.

In [12] introduces several approaches to minimize the residual stresses in DED processes are introduced by using different substrate designs. First, the decrease in sensitivity in the initial non-steady state prior to the initial deposition. Second, to increase the heat passing through the substrate in a predetermined amount of time, thereby decreasing the maximum temperature gradients. Lastly, optimizing the stiffness of the substrate and the mechanical constraints it introduces can result in large residual stresses and thermal deformations during the construction and cooling phases; therefore, increasing the stiffness of the substrate can further reduce residual stresses.

Before starting the AM process, the substrate was at least twice preheated, according to [23]. In addition to the reduced distortions caused by pre-heating, it was shown that the various layers of the component have an effect on the distortions. Analyzing the same structure with different numbers of layers revealed that the structure with 11 layers had significantly less distortion than the structure with one layer. However, 3 layers demonstrated greater distortion than 1. This study suggests that the number of layers may decrease beyond a certain threshold. This is due to the dissimilar temperatures of the component and the substrate. When only 1 layer is deposited, the temperature differences are noticeable, but they remain unchanged when 3 layers are added. However, the layer above has a great deal of energy flowing through it. As shown in *Figure 14*, when the substrate is heated, the energy flowing through due to conduction from the deposited layer to the substrate decreases as the distance between the deposited layer and the substrate increases.

Consequently, temperature difference is essential for reducing residual stresses. Increasing the substrate's temperature is a common method for achieving this, as previously mentioned.

The alternative is to reduce heat loss from the substrate. This can be achieved by applying thermal insulation to the bottom of the substrate. While doing so would not reduce the initial residual stresses for the first layer deposited on a cool substrate, it would increase the average temperature of the substrate, thereby reducing distortions in the final layers.

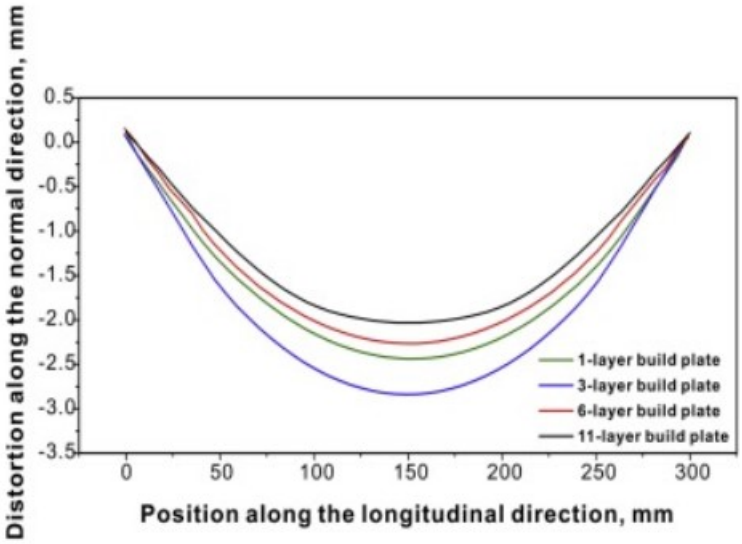

Figure 14: Distortions in the normal direction differ when comparing different layer builds[23]

2.7.5 Balancing layers

Utilizing a balancing layer on each built layer is one method of distortion mitigation, particularly for small components. This is accomplished through the sequential balancing layer and the alternating balancing layer. Both are based on balancing the longitudinal bending moment caused by the heat of the depositing layers, and the cooling of the deposition produces positive bending moments because the substrate and deposition contract, see *Figure 15*. Note that this method is suitable for unidirectional longitudinal layering since it is easily applicable to compensate for distortion in one direction [24].

To reduce distortions during the cooling phase, a sequential balancing layer perpendicular to the direction of the built layers is created to counteract the bending moment that the built layers have on the substrate. Alternately, the balancing layers are sequentially applied, first to one end of the substrate and then to the other.

Alternating balancing layers eliminate the need to sacrifice material on one end of the substrate in order to construct layers on the other. Consequently, the neutral axis of the substrate will remain balanced with respect to bending moments, resulting in the substrate remaining straight throughout the entirety of the fabrication process. Ultimately, the moment of bending caused by the balancing layer should equal the moment of bending of the actual layers.

A study done by [24] suggests that the alternating balancing layers are a sufficient method for mitigating distortions. Significant enough to eliminate 91% of the distortions compared to a technique that relies solely on substrate preheating.

2.7.6 Scanning pattern

Reduce the heat input, which is applicable for either scanning speed or feeding rate, to reduce the residual stresses further.In [25] studies the concept of modifying the scanning

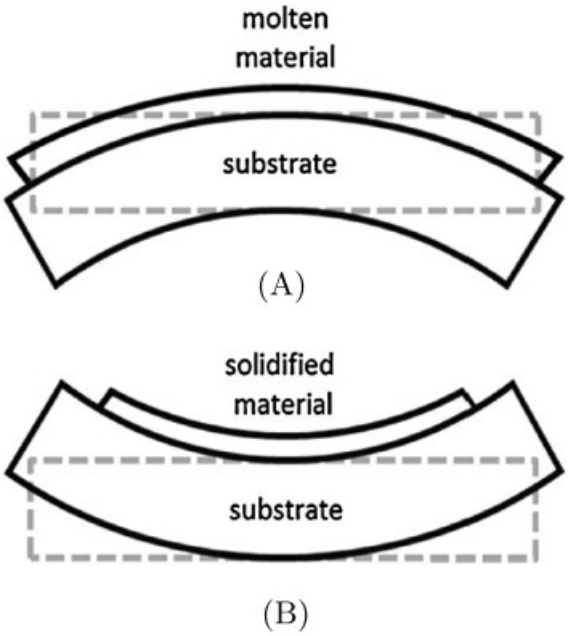

Figure 15: Simplified concept of the substrate and component bending after deposition and cooling [24]

pattern in multi-layer wire arc AM of Ti-6Al-4V by reducing the track length of the printing strategy. An example of a short track length can be done in rectangular components by depositing layers on the short side and only depositing in that direction throughout the whole build.

Consequently, the residual stresses were reduced by employing this strategy without allowing for any downtime between the deposition of each layer. *Figure 16* illustrates different scanning patterns, ranging from the short track, long track, and spiral, etc.

The substrate is significantly heated during this deposition, and the accumulated temperature gradient stabilizes after the third (out of a total of five) layer is deposited. Therefore, the difference in temperature between the third and fifth layers is negligible at the component's center. Additionally, the substrate was clamped, resulting in high compressive stresses due to upward deformations. In addition, when the long side is scanned, contraction will be predominant in that direction, resulting in significant tensile stresses in that direction and compressive stresses in the parallel direction. In conclusion, scanning along the shorter side reduces residual stresses [25].

2.7.7 Welding

Mitigation and distortion compensation for welding are sufficiently similar to be useful for enhancing AM modeling. Large structures undergo distortions during welding due to buckling caused by residual stresses. Consequently, it is preferable to reduce the residual stresses, for which there are multiple solutions.

The thermal tensioning technique has been validated and demonstrated to be advantageous for welding. Utilizing a steady-state temperature differential, a thermal strain is induced at the welding points prior to and throughout the welding process. This temperature difference remains constant as the welding process advances. However, it may be difficult to maintain a steady-state temperature difference, especially prior to the welding process;

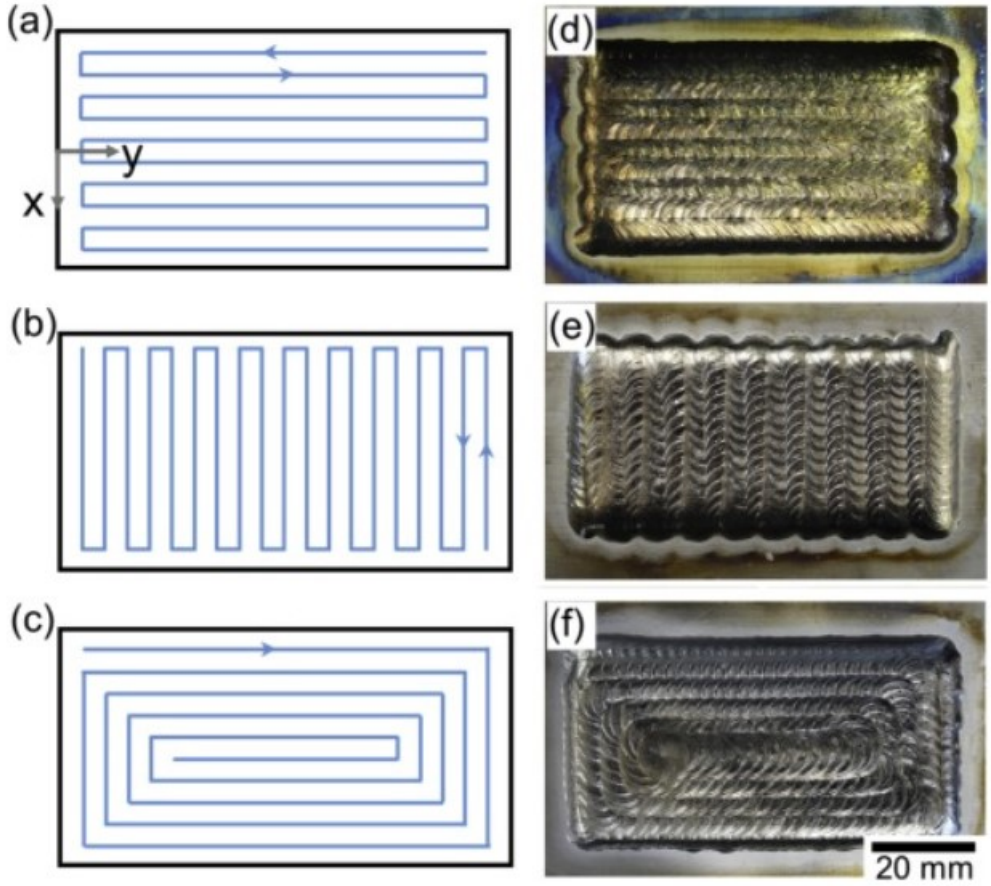

Figure 16: Different distortions results when applying different scanning patterns [25]

therefore, a transient solution may be advantageous. Despite the ineffectiveness of a parametric study due to the large number of variables to be considered, relocating heat sources can be aided by a sensitivity analysis with an iterative procedure. In conclusion, it has been demonstrated that this method of local thermal tensioning without any cooling produces components free of residual stresses in certain cases [26].

Differential heating has been proposed to reduce bowing distortion, and longitudinal bending. In contrast, buckling, bowing distortion, and angular change are caused by welding distortion, such as that of stiffeners. As the welding line does not coincide with the neutral axis of the structure, the welding process can result in significant longitudinal bending or bowing distortion during the production of T-type stiffeners. Therefore, the welding shrinkage and cooling will induce longitudinal bending, which is one of the out-of-plane distortions. *Figure 17* depicts the three in-plane and three out-of-plane distortion modes. Mitigation of this problem is possible with differential heating; meaning that parts are heated differently, some parts are preheated and cooled, and other parts are not preheated. This causes the preheated component to contract further, resulting in less longitudinal bending. However, once one part is preheated, production time will be reduced, making this a poor solution for parts containing numerous materials, such as long T-stiffeners [27].

In addition, it has been demonstrated that reducing the compressive stress during welding is appropriate for mitigating residual stresses and plastic strains, as discussed previously; one solution is thermal tensioning. Mechanical tensioning, which involves mechanically

stretching the plate during welding and resulting in a reduction of residual stresses when the load is released, is an alternative solution. This method has proven effective for thinner sections welded into thicker frames, but for thicker sections, the procedure may be challenging due to the need for heavier equipment and greater forces [27]. Therefore, tensile tensioning is preferred, with the application of tensile strains without a complex mechanical procedure.

Another solution that is considered useful for mitigating buckling distortion in welding is "weld cooling". This method has proven to be effective according to [28]. As the driving factor for residual stresses and distortion is the cooling stage of the welding; thus, optimizing the temperature field, once again, is a successful method in mitigating warpage. Some of the current solutions for changing the temperature field are applying high-speed airflow and cooling the welding structure by applying water.

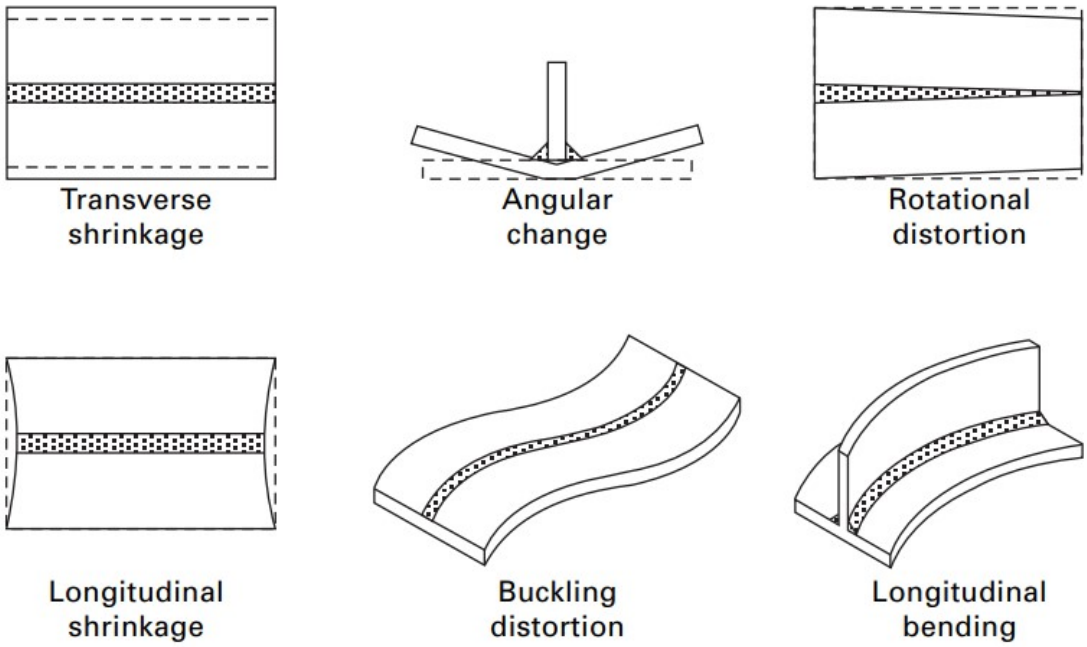

Figure 17: Different distortion modes

Considering welding, multi-pass welding is largely applicable to structural solutions. The procedure is relatively similar to the process of AM, with welding one layer at a time and letting the layer cool before applying the succeeding layer. Hence, altering distortions is clear, like AM, on layers previously applied[2]. In general, the solutions and techniques that have been most efficient are low heat-input welding, whereas heat is the determining factor for residual stresses; in other words, using laser beam welding or AM is a preferable solution [29].

Depending on the specific forming technique the defect may differ. [1] includes a general classification without regarding the specific technique, shown in *Figure 18* . Whereas warping may occur under fast heating and cooling cycles and the corrective measure is controlling the thermal history.

Nomenclature	Description	Origin (*process*)	Corrective measures
Bow, side and longitudinal bent	Sidewise or longitudinal bending	Inaccurate guiding or alignment in *rolling or slitting*	Use of levelling or straightening rolling
Buckling	Bending under compressive stresses	Any forming process: inaccurate stress distribution	Straightening
Camber	Curvature in rolled plates/strips	Roll bending at the middle of the rolls – *rolling*	Compensated by varying the roll diameter across the roll length
Cobbling	Accidental distortion in shape through re-rolling	Front end being caught and rolled again – *rolling*	Reduced rolling speed
Exfoliation	Disjoining during fabrication	Any forming process: pipes, unwelded blowholes, severe inclusion content	Control of solidification structure
Overfill/underfill	Inappropriate (over or under) metal flow	Extrusion/drawing: over or under feed of metal	Control of feed rate
Warping	Distortion or warpage	Any warm/hot forming: fast heating cooling	Control of thermal history

Figure 18: General classification of distortion modes and their respective correction [1]

3 Thermal-Mechanical Model

The utilized TM model is a three-dimensional coupled visco-plastic-elastic-plastic model. The coupled model assumes that the FE discrete analysis is first used to simulate a thermal problem, and then the thermal simulations are used for the mechanical calculation.

In the subsequent sections, the governing equations for TM modeling will be presented, along with the relevant Dirichlet and Neumann boundary conditions, heat source definitions, and approximations. The following equations are derived from previous works of authors working on the same *in-house* software [9] [30].

3.1 Thermal Model

3.1.1 Strong form

AM is performed in two stages: printing and cooling. Both thermal phases are governed by the *balance of energy equation* which is defined as:

$$\dot{H} = -\nabla \cdot \mathbf{q} + \dot{Q} + \dot{D}_{\text{mech}} \tag{1}$$

where $\dot{H}$is the enthalpy rate (per unit of volume), while $\dot{Q}$ and $\dot{D}_{\text{mech}}$ represent the heat source (per unit of volume) and the thermo-mechanical dissipation rate (per unit of volume), respectively. $\mathbf{q}$ is the heat flux which can be expressed as a function of the temperature gradient through Fourier's law as:

$$\mathbf{q} = -k\nabla T \tag{2}$$

where *k(T)* is the (temperature dependent) thermal conductivity.

Before integrating the *energy balance equation*, see *Equation 1*,the enthalpy state variable, $\dot{H}$, is to be expressed as a function of the temperature, T, and the liquid fraction, f_{L}, and, therefore, the enthalpy rate can be defined as:

$$\dot{H}(T, f_{\text{L}}) = \frac{\partial H}{\partial T}\dot{T} + \frac{\partial H}{\partial f_{\text{L}}} = C\dot{T} + L\dot{f}_{\text{L}} \tag{3}$$

where $C(T) = \frac{\partial H}{\partial T}$ is the temperature dependent heat capacity and $L = \frac{\partial H}{\partial f_{\text{L}}}$ is the latent heat that is released during the phase-change process. The weak form can be derived.

3.1.2 Weak form

Let V be an open and bounded domain in $\mathbb{R}^{n_{\text{dim}}}$. Where n_{dim} is the number of dimensions of the space, closed by the smooth boundary $S = S_{\text{T}} \cup S_{\text{q}}$, where the corresponding boundary conditions are defined in terms of either prescribed Dirichlet (temperature on S_{T} or Neumann (heat flux), S_{q} boundary conditions, this is illustrated by *Figure 19*.

Then after introducing a test function into the energy balance equation, *Equation 1*, expressed as a variation of the temperature field δT will result in the following expression:

$$\int_{\text{V}} \left[\dot{H}\delta T\right] dV = -\int_{\text{V}} \left[(\nabla \cdot \mathbf{q})\delta T\right] dV + \int_{\text{V}} \left[(\dot{Q} + \dot{D}_{\text{mech}})\delta T\right] dV \tag{4}$$

By applying the chain derivation role for expression: $\int_{\text{V}} [(-\nabla \cdot \mathbf{q})\partial T]$, and then substituting this expression, with Fourier's law,*Equation 2*, final resultin the following expression:

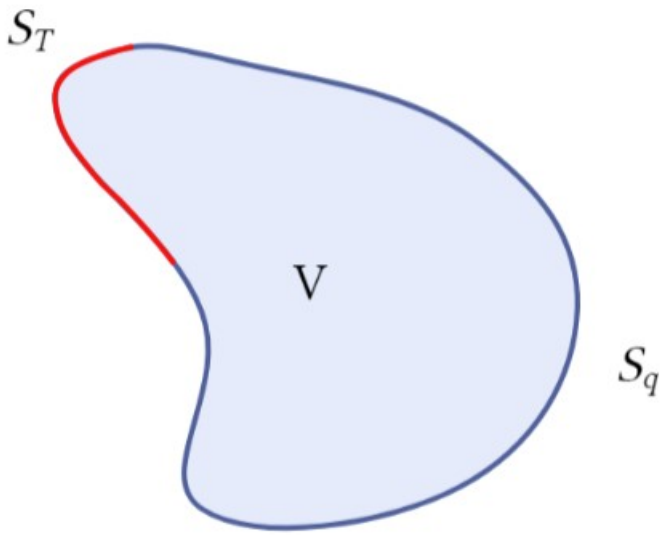

Figure 19: Open and bounded domain, V

$$\int_{\mathrm{V}} \left[(\rho C \dot{T} + L \dot{f}_{\mathrm{L}}) \delta T \right] dV + \int_{\mathrm{V}} \left[k \nabla T \cdot \nabla (\delta T) \right] dV = W^{ext}_{\mathrm{therm}} \quad \forall \delta T \tag{5}$$

where, W^{ext}_{ther} denotes the external work of the thermal loads:

$$W^{ext}_{\mathrm{ther}}(\delta T) = \int_{\mathrm{V}} \left[\left(\dot{D}_{\mathrm{mech}} + \dot{Q} \right) \right) \delta T \right] dV - \int_{\mathrm{Sq}} \left[(\bar{q} + q_{\mathrm{cond}} + q_{\mathrm{conv}} + q_{\mathrm{rad}}) \, \delta T \right] dV \tag{6}$$

where, $\bar{q}$ is the prescribed heat flux, heat loss by convection q_{conv}, heat flux by conduction q_{cond}, and the radiation heat flux q_{rad}. First, the heat loss due to the heat conduction process between the component and the clamping system can be expressed by Newton's law:

$$q_{\mathrm{cond}} = h_{\mathrm{cond}}(T - T_{\mathrm{clamp}}) \tag{7}$$

The heat losses resulting from convection is expressed similarly:

$$q_{\mathrm{conv}} = h_{\mathrm{conv}}(T - T_{\mathrm{env}}) \tag{8}$$

where, h_{conv} is the temperature dependent heat transfer coefficient (HTC) by convection, and it is dependent on the geometry of the component. T_{env} is the temperature of the environment.

The Stefan–Boltzmann radiation law describes heat loss due to radiation:

$$q_{\mathrm{rad}} = \varepsilon_{\mathrm{rad}} \sigma_{\mathrm{rad}} (T^4 - T^4_{\mathrm{env}}) \tag{9}$$

where, $\varepsilon_{\mathrm{rad}}$ is the surface emissivity. σ_{rad} is the Stefan–Boltzmann constant.

3.2 Mechanical Model

3.2.1 Strong form

The mechanical problem is governed by the balance of momentum equation. The strong form, for quasi-static conditions, can be stated as: find the displacement field, $\mathbf{u}$, for given (prescribed) body forces $\mathbf{b}$, such that:

$$\nabla \cdot \boldsymbol{\sigma}(\boldsymbol{u}) + \mathbf{b} = 0 \tag{10}$$

The stress tensor can be split into a hydrostatic part and a deviatoric part, p and $\mathbf{s}$, respectively:

$$\boldsymbol{\sigma}(\mathbf{u}, p) = p\mathbf{I} + \mathbf{s}(\mathbf{u}) \tag{11}$$

where, $p = \frac{1}{3}tr(\boldsymbol{\sigma}$ and $\mathbf{s} = dev(\boldsymbol{\sigma})$. This split is convenient when dealing with when the deformations are mostly deviatoric, which is a characteristic of the liquid phase. With this, the strong form can be rewritten:

$$\nabla \cdot \mathbf{s}(\mathbf{u}) + \nabla p + \mathbf{b} \tag{12}$$

$$(\nabla \cdot \mathbf{u} - e^T) = \frac{p}{K} \tag{13}$$

where e^T is the thermal deformation and K(T) is the temperature dependent bulk modulus which controls the material compressibility. This formulation is denoted as the $\mathbf{u}$/p formulation, or the mixed formulation. With this split, it is suitable to do both incompressible as compressible cases. In particular, when the material is liquid the bulk modulus goes to infinity, $K \to \infty$. So that *Equation 12* enforces the volumetric constraint as:

$$\nabla \mathbf{u} = e^T \tag{14}$$

Like the thermal problem, the expressions have to be integrated over the volume domain V being S the corresponding boundary $S = S_\sigma \cup S_\mathrm{u}$ where tractions are prescribed on S_σ, while displacements are specified on S_u.

3.3 Weak form

The weak form of the mechanical problem with the mixed $\mathbf{u}$/p formulation in *Equation 12* and *Equation 13* is:

$$\begin{cases} \int_\mathrm{V} \left[(\nabla \cdot \mathbf{s}(\mathbf{u}) \cdot \delta\mathbf{v})\right] dV + \int_\mathrm{V} (\nabla p \cdot \delta\mathbf{v}) dV + \int_\mathrm{V} (\mathbf{b} \cdot \delta\mathbf{v}) dV = 0 \quad \forall \delta\mathbf{v} \\ \int_\mathrm{V} \left[(\nabla \cdot \mathbf{u} - e^T - \frac{p}{k})\delta p\right] dV = 0 \quad \forall \delta p \end{cases} . \tag{15}$$

where, $\delta\mathbf{v}$ and δp are the variations of the displacements and pressure field, respectively. Integrating by parts results in:

$$\int_\mathrm{V} \left[\nabla \cdot \mathbf{s}(\mathbf{u})) \cdot \delta\mathbf{v}\right] dV + \int_\mathrm{V} (\nabla p \cdot \mathbf{v}) dV = -\int_\mathrm{V} (\mathbf{s}(\mathbf{u}) : \nabla^s \delta\mathbf{v}) dV - \int_\mathrm{V} (p\nabla \cdot \delta\mathbf{v}) dV + \int_{\mathrm{S}_\sigma} (\bar{\mathbf{t}} \cdot \delta\mathbf{v}) dS \tag{16}$$

where $\bar{t}$ are prescribed tractions on S_σ. Substituting *Equation 16* into *Equation 15*, the mixed **u**/p variation form of the quasi-static mechanical problem denotes:

$$\begin{cases} \int_{\mathrm{V}} (\mathbf{s}(\mathbf{u}) : \nabla^s \delta\mathbf{v}) dV + \int_{\mathrm{V}} (p \nabla \cdot \delta\mathbf{v}) dV = W^{ext}_{\mathrm{mech}} \\ \int_{\mathrm{V}} \left[(\nabla \cdot \mathbf{u} - e^T - \frac{p}{K}) \delta p \right] dV = 0 \end{cases} . \tag{17}$$

where, W^{ext}_{mech} denotes the external work of the mechanical loads, which is defined as:

$$W^{ext}_{\mathrm{mech}}(\delta\mathbf{v}) = \int_{\Omega_\chi} (\mathbf{b} \cdot \delta\mathbf{v}) dV + \int_{\delta\Omega_\sigma} (\bar{\mathbf{t}} \cdot \delta\mathbf{v}) dS \tag{18}$$

3.4 Mechanical constitutive laws

The model employed must take into consideration wide ranges of temperatures that appear during the AM process, where the temperatures range between room temperature and significantly high values beyond melting temperature. Thus, the response must include elasto-plastic behavior at room temperature and pure viscous over melting point. This can be done, as already stated, by adopting an apropos elasto-plastic-visco-plastic model. When the temperature increases and closes to the melting point the viscous behavior becomes predominant, and the elastic limit reduces, vanishing when liquidus temperature is reached. Consequently, a purely viscous model is recovered for the liquid-like phase.

The constitutive laws for all temperature ranges of the process is specified by a J2-thermo-elasto-visco-plastic constitutive model:

$$p = \frac{K}{f_{\mathrm{S}}} (e^{vol} - e^T) \tag{19}$$

$$\mathbf{s} = \frac{2G}{f_{\mathrm{S}}} (\mathbf{e} - \mathbf{e}^{vp}) \tag{20}$$

where G(T) is the temperature dependent shear modulus and K(T) is the temperature dependent bulk modulus which stands for the material compressibility.

The total strain tensor is computed in terms of the displacement field, **u**, as:

$$\boldsymbol{\varepsilon}(\mathbf{u}) = \nabla^s \mathbf{u} \tag{21}$$

and its volumetric and deviatoric parts are obtained as:

$$e^{vol} = tr(\boldsymbol{\varepsilon}) = \nabla \cdot \boldsymbol{u} \tag{22}$$

$$\mathbf{e} = dev(\boldsymbol{\varepsilon}) = \boldsymbol{\varepsilon} - \left(\frac{e^{vol}}{3} \right) \mathbf{I} \tag{23}$$

The thermal deformation $e^T(T)$ is defined as a volumetric term of the form:

$$e^T(T) = e^{cool}(T) + e^{pc}(T) \tag{24}$$

where, $e^{cool}(T)$ is the thermal dilatation experimented by the material from the initial temperature T_0 to the current temperature T, while $e^{pc}(T)$ is the thermal shrinkage characteristic of the liquid-to-solid phase transformation. The thermal expansion denotes:

$$e^{cool} = 3\left[\alpha(T)(T - T_{\text{env}}) - \alpha(T_0)(T_0 - T_{\text{env}})\right] \tag{25}$$

where $\alpha(T)$ is the temperature dependent secant thermal expansion coefficient, and T_{env} is the room temperature. The thermal shrinkage is due to the variation in density in the solidification interval $T_{\text{S}} \leq T \leq T_{\text{L}}$:

$$\frac{de^{pc}}{dt} = -\frac{1}{\rho}\frac{d\rho}{dt} \tag{26}$$

Integrating the *Equation* above, results in:

$$e^{pc}(T) = \ln\frac{\rho_0}{\rho(T)} \cong \frac{\rho_0 - \rho(T)}{\rho_0}, \quad T_{\text{S}} \leq T \leq T_{\text{L}} \tag{27}$$

where, ρ_0 is the value of the density at the initial temperature, with the restrictions:

$$\begin{aligned} \rho_0 &= \rho_{\text{S}}, \quad T_0 \leq T_{\text{s}} \\ \rho_0 &= \rho_{\text{L}}, \quad T_0 \geq T_{\text{L}} \end{aligned} \tag{28}$$

where, $\rho_{\text{S}} = \rho(T_{\text{S}})$ and $\rho_{\text{L}} = \rho(T_{\text{L}})$ are the material densities at solidus and liquidus temperatures.

Now a temperature dependant J2-yield-surrface $\Phi(\mathbf{s}, q_{\text{h}}, T)$ can be introduced as:

$$\Phi(\mathbf{s}, q_{\text{h}}, T) = \| \mathbf{s} \| - f_{\text{S}} R(q_{\text{h}}, T) \tag{29}$$

where, $R(q_{\text{h}}, T)$ is the temperature dependent yield-surface radius, defined as:

$$R(q_{\text{h}}, T) = \sqrt{\frac{2}{3}}\left[\sigma_{\text{y}}(T) - q_{\text{h}}\right] \tag{30}$$

where, $\sigma_{\text{y}}(T)$ is the temperature dependent initial yield stress parameter,and the stress-like variable, $q_{\text{h}}(\xi, T)$, conjugate to the isotropic strain-hardening variable, ξ, controls the isotropic hardening effect defined:

$$q_{\text{h}}(\xi, T) = -\left[\sigma_{\infty}(T) - \sigma_{\text{y}}(T)\right]\left[1 - e^{-\delta(T)\xi}\right] - h(T)\xi \tag{31}$$

where, $h(T)$ and $\delta(T)$ are the coefficients which control the linear and the exponential isotropic hardening laws and, σ_{∞} is the temperature dependent saturation flow stress parameter. The visco-plastic strains, ε^{vp} are considered purely deviatoric $\boldsymbol{\varepsilon}^{vp} = \boldsymbol{e}^{vp}$. Their definition can be derived from the principle of maximum plastic dissipation together with the evolution law of the isotropic strain-hardening variable, ξ, defined as:

$$\dot{\boldsymbol{e}}^{vp} = \dot{\gamma}^{vp}\frac{\partial\Phi(\mathbf{s},q,T)}{\partial\mathbf{s}} = \dot{\gamma}^{vp}\frac{\mathbf{s}}{\parallel \mathbf{s} \parallel} = \dot{\gamma}^{vp}\mathbf{n} \tag{32}$$

$$\dot{\xi} = \dot{\gamma}_{\mathrm{vp}}\frac{\partial\Phi(\mathbf{s},q_{\mathrm{h}},T)}{\partial q_{\mathrm{h}}} = \dot{\gamma}^{vp}\sqrt{\frac{2}{3}}f_{\mathrm{S}} \tag{33}$$

where $\mathbf{n} = \frac{\partial\Phi(s,q,T)}{\partial\mathbf{s}} = \frac{\mathbf{s}}{\|\mathbf{s}\|}$ is the normal to the yield surface. The visco-plastic multiplier, $\dot{\gamma}_{\mathrm{vp}}$, is computed assuming a rate-dependent evolution law as described below:

$$\dot{\gamma}^{vp} = \left\langle \frac{\Phi(\mathbf{s},q_{\mathrm{h}},T)}{\eta} \right\rangle^{\frac{1}{m}} \tag{34}$$

where $\langle\,\cdot\rangle$ represents the Macaulay brackets. Thus, it is possible to experience a viscous overstress, $\eta(\dot{\gamma}_{\mathrm{vp}})^m$, whcih is allowed to exceed the yield surface, being $\eta(T)$ the temperature dependent plastic viscosity, and $m(T)$ its temperature dependent rate sensitivity. The resulting equivalent stress yields:

$$\sigma_{\mathrm{eq}} = \sqrt{\frac{3}{2}}\left[f_{\mathrm{S}}R + \eta(\dot{\gamma}^{vp})^m\right] \tag{35}$$

3.4.1 Solid Phase

Depending on which phase the material is in (which is dependent on the temperature), there will be some formulations that are separate. First, the solid phase, which is straight-forward, $T < T_{\mathrm{S}}$ and $f_{\mathrm{S}} = 1$:

$$p = K(e^{vol} - e^{T}) \tag{36}$$

$$\mathbf{s} = 2G(\boldsymbol{e} - \boldsymbol{e}^{vp}) \tag{37}$$

where the evolution laws for the visco-plastic strains and the isotropic hardening are deduced *Equation 32* and *Equation 33* as for the classic J2-thermo-elasto-visco-plastic model.

3.4.2 Liquid-like Phase

The liquid like phase implies the incompressibility constraint, as shown before, $K \to \infty$, applies to the melted material. This is characterized above the liquidus temperature: $T > T_{\mathrm{L}}$ and $f_{\mathrm{S}} = 0$. Both the elastic and deviatoric strain tensor vanish components from *Equations 19* and *20*, and the volumetric deformation is equal to the thermal deformation: $e_{\mathrm{vol}} = e^{T}$. This corresponds to the *continuity equation for mass conservation*:

$$\nabla\cdot\mathbf{u} - e^{T}(T) = 0 \tag{38}$$

On the other hand, *Equation 20* reduces to:

$$\boldsymbol{e} = \boldsymbol{e}^{vp} \tag{39}$$

Thus, only viscous shear deformations take occur. The yield-surface radius defined in *Equation 30* reduces as the temperature increases till vanishing (R=0) above the liquidus temperature. Introducing this result into the evolution law of the plastic multiplier, (*Equation 34*), a purely viscous model is recovered:

$$\mathbf{s} = \eta(\dot{\gamma}^{vp})^{m-1}\dot{\boldsymbol{e}}^{vp} \tag{40}$$

3.4.3 Mushy phase

The material model provides a smooth transition from liquid-like to solid behavior as a function of the solid fraction function, $0 < f_S < 1$in the temperature range $T_S < T < T_L$. Observe that the yield stress vanishes in this temperature range. The elastic strains become insignificant compared to the visco-plastic deformations. Thus, the mushy phase is actually governed by the visco-plastic flow.

4 Methodology

During the review of the geometrical-distortion compensation and conventional mitigation strategies, it became clear that the distortion can be significantly reduced depending on the method. However, the literature on geometrical compensation only implemented the method of modifying the mesh and not the GCode; and from the mesh, both an STL file and GCode can be generated. This solution is needlessly complex and ineffective. Therefore, a more effective algorithm that instantly modifies the GCode should be created.

Additionally, this approach makes sense economically compared to more traditional approaches like pre-heating the substrate or using balancing layers, for instance. Since the method does not require supplementary material or additional expenses for the manufacturing process.

The use of GCode instead of a CLI is preferred in this case because GCode provides the flexibility to not only modify geometrical parameters, but also other critical parameters such as dwell time and speed. These additional parameters are important when simulating industrial components with complex geometries, which require precise control over the manufacturing process to achieve accurate results. The GCode, therefore, provides a more comprehensive and versatile approach to simulating these components, compared to a CLI which only allows for modification of limited parameters.

4.1 Distortion compensation algorithm

A Python algorithm was developed to modify the GCode for the distortion compensation portion. Using the internal software's calculated displacement field in conjunction with the original GCode, the scanning strategy is modified to partially compensate for the distortion. The current issue is that the employed FE method employs an automatic mesh generation with cubic boxes, resulting in nodes whose positions deviate from the nominal scanning pattern. The algorithm must therefore calculate information between the scanning pattern and nodes by interpolating and utilizing the Euclidean distance between the points, which is demonstrated below as a function in Python:

```python
def getClosestGcodePoint(meshPoint, gcodePoints):
    """
    Given a mesh point and a list of gcode points, finds the closest
↪   gcode point to the mesh point
    by calculating the euclidean distance between the mesh point and
↪   each point in gcodePoints.
    """
    # Use numpy to calculate euclidean distance between meshPoint and
    ↪  each point in gcodePoints
    distances = np.linalg.norm(gcodePoints - meshPoint, axis=1)
    # Find the index of the closest point in gcodePoints
    idxClosest = np.argmin(distances)
    # Return the closest point and its index in gcodePoints
    return gcodePoints[idxClosest], idxClosest
```

This function can therefore be used to create a dictionary with the GCode coordinates and the index of the closest points, where the value is a tuple of the closest points and the index, and this will later be used for calculating the average displacement for every given

mesh point.

```
def find_closest_points(reference_nodes, target_points):
    """
    Given a list of reference_nodes and a list of target_points, finds
↪   the closest point from target_points for each reference_node.
    Returns a dictionary where key is the reference_node and the value
↪   is a tuple of closest point and its index in target_points
    """
    result = []
    closest_indices = []
    for i in range(len(reference_nodes)):
        closest_point, closest_index =
        ↪  getClosestGcodePoint(reference_nodes[i], target_points)
        result.append(closest_point)
        closest_indices.append(closest_index)
    return result, closest_indices
```

Referring to *Section 3*, the displacement field, $(\overline{u})$, is first obtained through a TM simulation. The algorithm then reads the GCode and the coordinates of the hatch points and appends them to the output. Using the minimum Euclidean distance, the coordinates of the nodes and the coordinates of the hatch points can be matched and connected using these two dictionaries. Inverting the displacement field now permits the modification of coordinates:

$$\begin{cases} X_1 = X_0 - \overline{u}_{\mathrm{x}} \\ Y_1 = Y_0 - \overline{u}_{\mathrm{y}} \end{cases} . \tag{41}$$

In this study, the algorithm for compensation only addresses the X and Y displacement and does not consider Z-displacement. However, the inverted mesh methodology takes into account the Z-displacement. This is because the Z coordinates of the GCode and machinery represent the position of the layer, and thus, modifying the position of multiple points and having different heights for the same layer is not practical due to the gravity-induced deformation of the component. After modifying the coordinates, they must be replaced with the original coordinates or hatchlines, without altering the order or any other code. This ensures that the GCode can be printed and utilized for simulation after the replacement. A more detailed explanation of the Python methodology is shown in *Figure 20*. Additionally, the most important aspects and functions of the geometric compensation algorithm in Python are also presented in the Annex.

For the mesh modification part, the following steps are required for compensation:

1. Create the component in an STL file.
2. From the STL file run a TM simulation in the *in-house software*
3. Modify the position of the nodes according to the displacement field obtained
4. Slice the new STL file using a Slicer (Ultimaker Cura) to obtain a GCode
5. Run a TM simulation using the new GCode
6. Compare positions of the distorted geometry with the nominal geometry from the original STL file

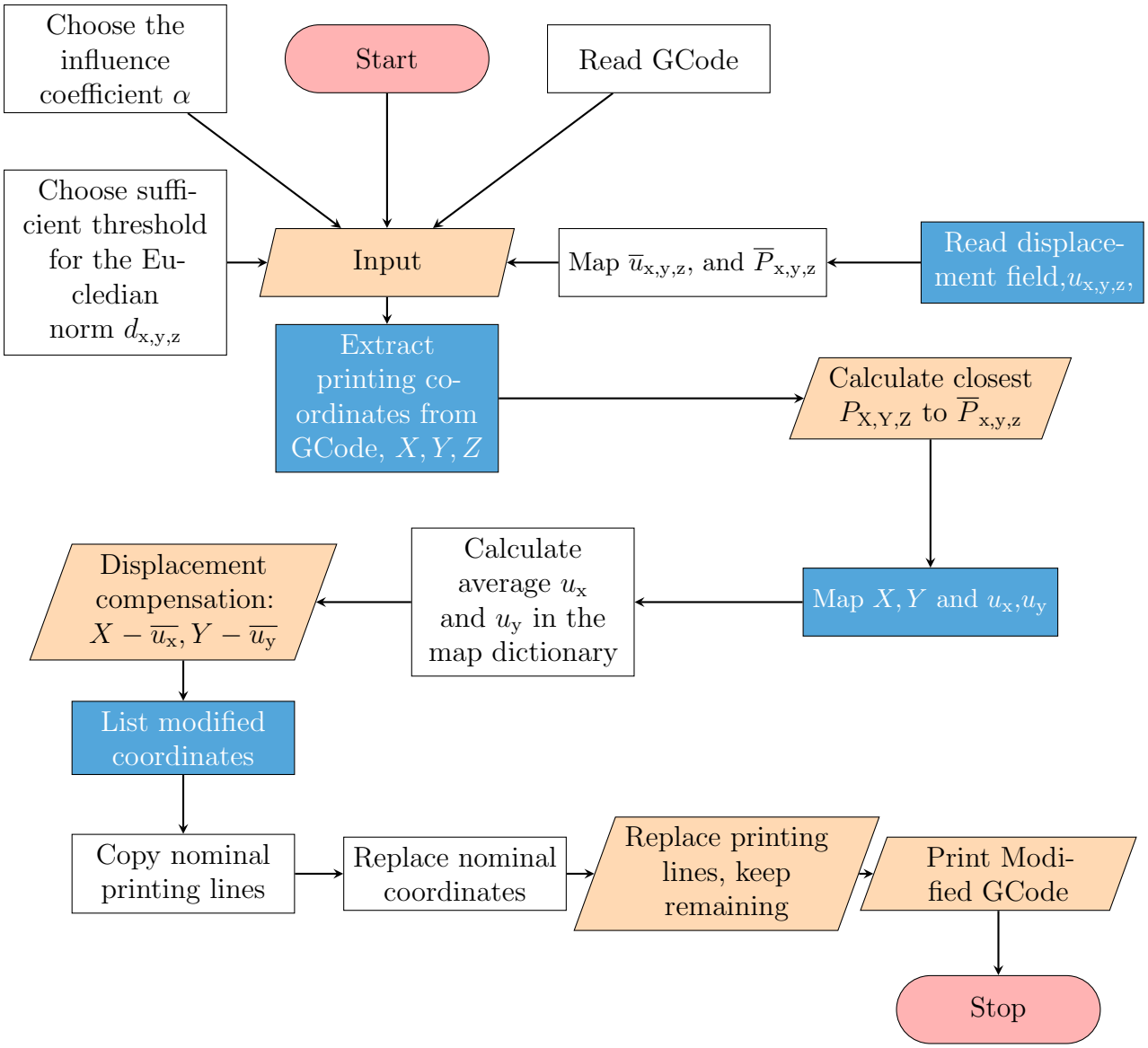

Figure 20: Geometric-distortion compensation algorithm

4.2 Iterative process

The entire procedure of obtaining the displacement field from a TM simulation, modifying the GCode, and rerunning the simulation with the modified code can be accomplished in cycles. The GCode modification procedure is depicted in *Figure 21*. After the initial simulation and compensation, the user will be able to repeat the process or end it.

Since the mesh is automatically generated, it will not adhere to the nominal geometry, resulting in different meshes. Therefore, running the compensated part in a loop could cause the geometry to deviate from the desired geometry, in an uncontrolled manner. Therefore, this will not be done for the algorithm.

However, the loop of compensating the same mesh will be done with manual mesh generation, with the tetrahedral elements used for the impeller case. A STL file will be generated following the discovery of a satisfactory result, one that exhibits nearly zero distortions for mesh compensation. With the modified geometry or modified STL file, the Slicer software can generate a GCode. This GCode can therefore be used to simulate a case with automatic mesh generation, and it will be compared to the algorithm to determine

which method is superior, the algorithm or the mesh compensation.

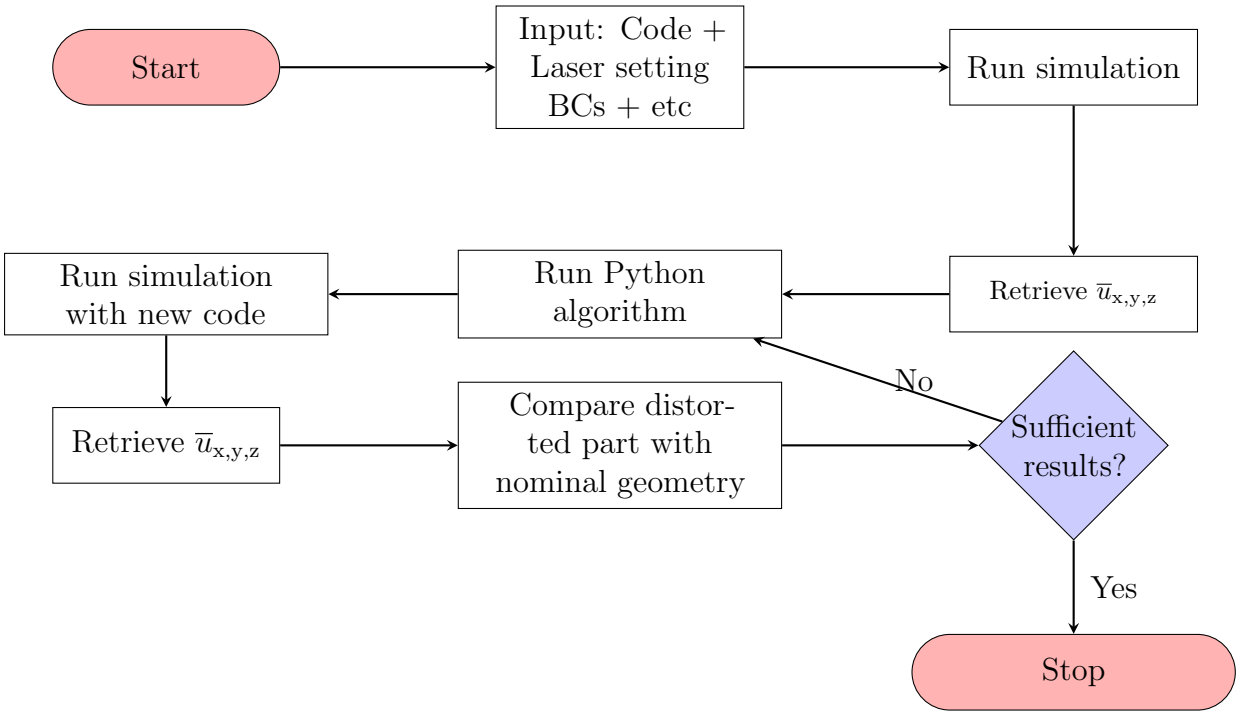

Figure 21: Iterative process of the compensation procedure

4.3 Threshold

Depending on the geometry of the part, the type of AM process, and the scanning pattern, the threshold used to identify displacements of interest in the GCode varies. Determining a satisfactory threshold for significant Euclidean displacements requires iterations. In most cases the threshold will be used to locally modify the GCode, for example at the wings of an impeller, see *Figure 27*.

This is done because at the body of the components, the distortions will mostly be due to gravitational forces,(and even though the average temperature are larger at the body of the component, the distortions will be smaller due to the rigidity). However, the X and Y-displacements are significant at the less rigid parts, such as the compressor's thin blades. As a result, this location becomes much more interesting because the algorithm involves changing the X- and Y-displacement. *Table 2* provide the threshold used for each case

Table 2: Threshold used for the algorithm, for each case

Case	Threshold (mm)
Large impeller	0.5
Small impeller	0.3
Gear	0.18
Compressor	2.5

4.4 Automatic mesh generation

A mesh can be generated automatically using a GCode and a mesh generation procedure. This method is appropriate for the AM to represent the actual manufacturing process without requiring the engineer to decipher the GCode to a manual mesh generated from a CAD file. In addition, the method of comparing modified GCodes to the original GCode

after distortion compensation makes mesh generation efficient in terms of the iterative process of reducing distortions.

4.5 Model

The AM method used will be the LBPF process with a layer-by-layer computational process, since several iterations with several geometrical models will be used the approach should be low-fidelity. Already discussed, LPBF are suitable for very complex geometries, like an impeller or compressor.

4.5.1 Geometry

All the cases used for the analysis are industrial cases with different purposes. Two impellers, one small, see *Figure 22b* and one large, see *Figure 22d*.

Also, a compressor is used, see *Figure 22a*, this case is the most complex with very thin walls that bend at the top and a large inclined body. Hence, the component will suffer significant bending at the thin walls/wings, and this case will both be used the algorithm, however as it was created on FREECAD it could be used to compute the distortions with a manual mesh and thus using that displacement field for the algorithm.

The last case is a gear, illustrated in *Figure 22c*, with a large rigid body, the distortions will act differently compared to the impeller and the compressor. It will be used to assess the accuracy of the algorithm in general. *Table 3* provides information regarding the height, layer size for each model.

Table 3: Geometrical parameters for each case

Case	Layer size (mm)	Height (mm)
Large impeller	0.5	50
Small impeller	0.5	20
Gear	0.5	72
Compressor	0.5	200

4.5.2 Material

The material used is the alloy Ti-6AI-4V, where the material properties used, and saturation laws are elasto-plastic, see *Section 3* for the governing equations. Material properties for the alloy Ti-6AI-4V is illustrated by the graphs in *Figure 23*.

The isotropic hardening laws are a combination of the saturation law and the linear hardening equation, which is presented in *Section 3*. *Table 4* demonstrates the plastic material properties throughout the thermal history, the saturation law and linear hardening. The plastic behaviour are utilized with saturation and hardening laws according to *Equation 31*.

Table 4: Plastic properties for alloy Ti-6AI-4V

$T(^{\circ}C)$	Saturation flow stress (Pa)	Linear hardening (Pa)
20	$1154e^6$	$800e^6$
200	$925e^6$	$800e^6$
400	$656e^6$	$800e^6$
600	$646e^6$	$300e^6$

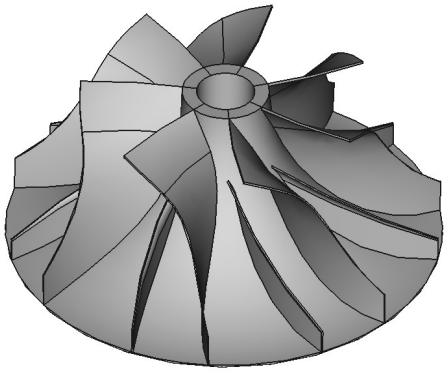

(a) STL file of the compressor

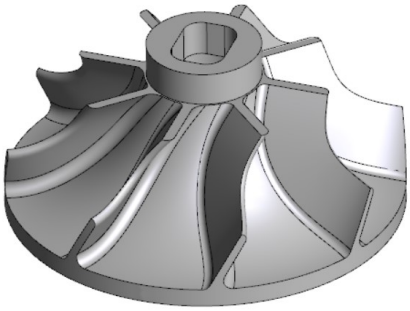

(b) STL file of the smaller impeller

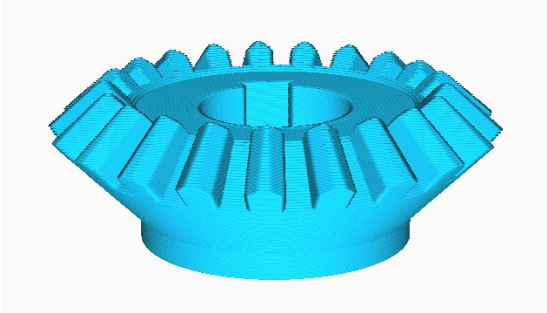

(c) Preview of GCode of the gear

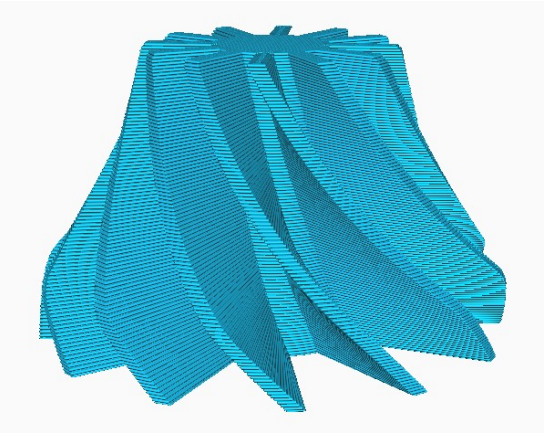

(d) Preview of GCode of the impeller

Figure 22: The four different models used in the analysis

4.5.3 Finite element discretization

The quality of the mesh is illustrated in *Figure 24d* for the impeller, with a finer discretization for the component and a lower refinement level for the fixed substrate. It is necessary to use a fixed clamp on the whole substrate to fix the bottom of the component. This will make the computational time slower since the substrate must be used for the entire analysis and every time-step. The same mesh refinement and choice goes for the compressor, and gear.

The mesh is generated automatically, and the mesh size should at least be equal to the layer size. For all cases, this will be **0.5mm** element size in all directions.

Since the impeller, as shown in *Figure 24d*, is quite large, and simulating it with manual mesh generation can be time-consuming and complex. To make the process more manageable, a smaller impeller will be used for the geometric compensation of the mesh procedure. As seen in *Figure 24b*, the mesh of the small impeller consists of around 250k tetrahedral elements. The use of tetrahedral elements is appropriate for this component due to its geometrical resolution, whereas using hexahedral elements would result in flawed surface replication.

In addition to using tetrahedral elements for the small impeller, they are also used in both the manual and automatic mesh generation processes for the simulation of the compressor case. This is because the compressor case requires a high degree of computational time and resources due to its size, and thus the mesh modification procedure was deemed impractical.

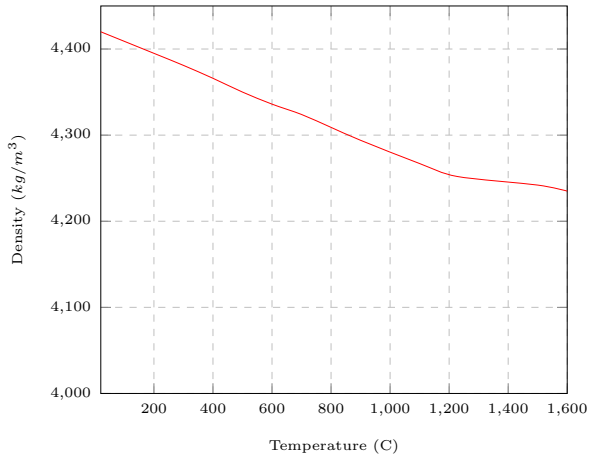

Density

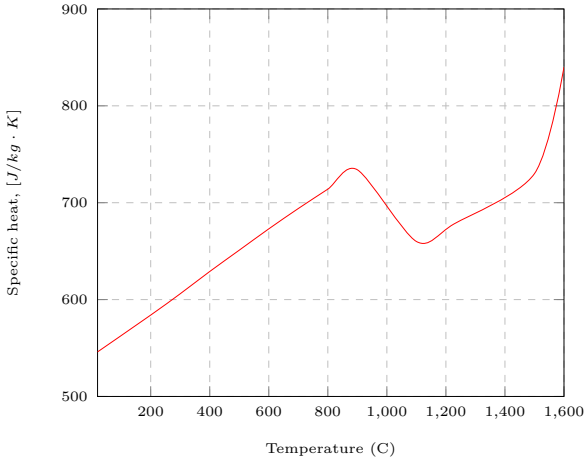

Specific heat

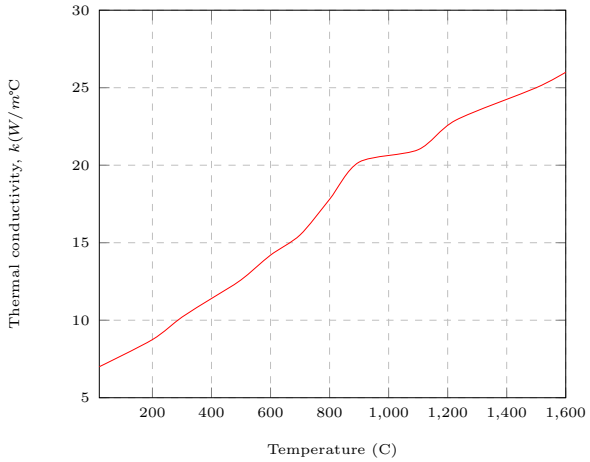

Thermal conductivity

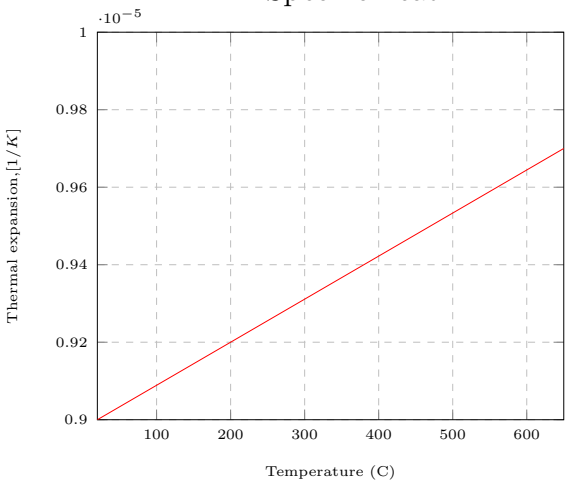

Thermal expansion

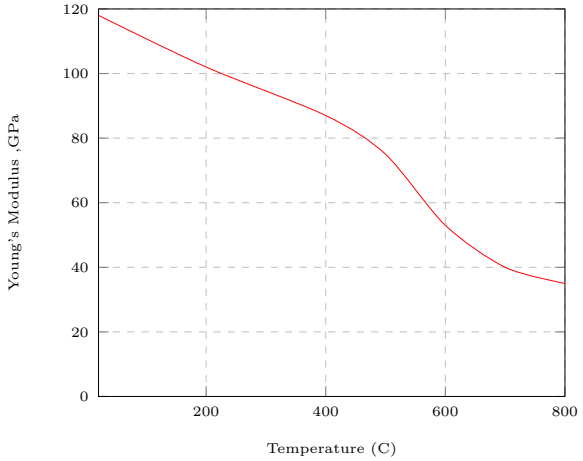

Young's Modulus

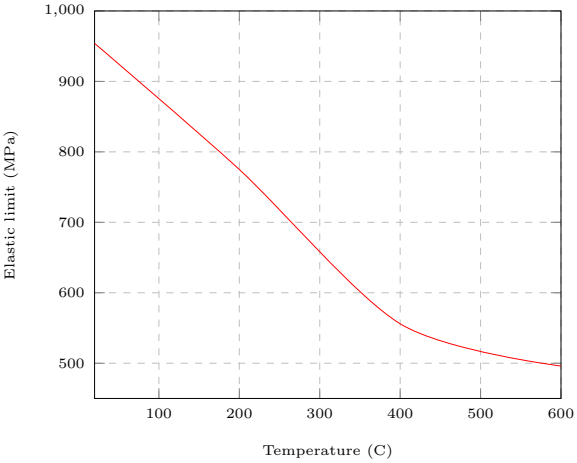

Elastic limit

Figure 23: Material properties for the alloy Ti-6AI-4V

The use of tetrahedral elements provides an optimal balance between computational efficiency and accuracy for this specific case. It is important to note that the choice of the mesh elements depends on the complexity of the geometry and the simulation requirements, in this case tetrahedral elements provide a good balance but it could be different for other cases.

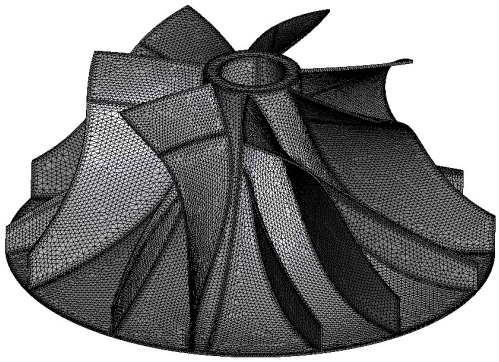

(a) Mesh of the compressor with cubic boxes, the substrate is not illustrated for clarity

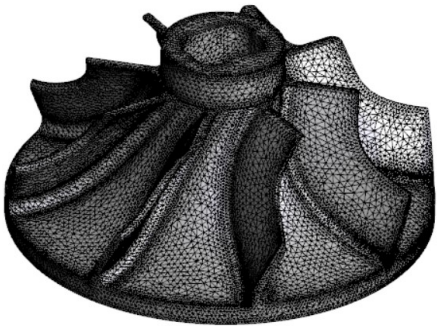

(b) Triangular mesh of the smaller imepller

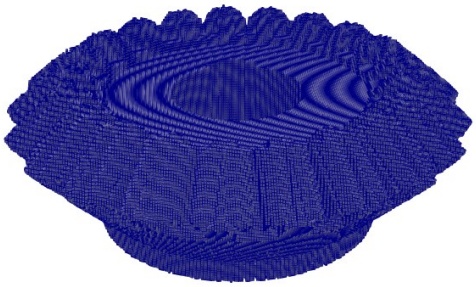

(c) Mesh of the gear with cubic boxes, the substrate is not illustrated for clarity

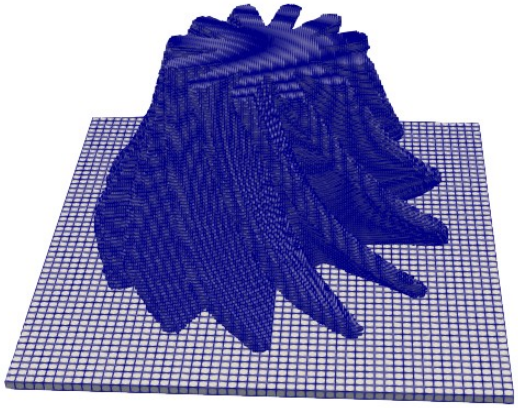

(d) Mesh of the impeller with cubic boxes

Figure 24: The different models with corresponding meshes

4.5.4 Time-step strategy

Using layer-by-layer time-stepping, the approach for all cases is of low fidelity. When simulating with one of the *in-house* softwares that is used to generate an automatic mesh, one time-step uses cooling and printing in the same step as an average. Consequently, the temperature displayed in the simulation is the average temperature throughout the entire time-stepping. In contrast, the other *in-house* software employs two distinct time steps, one for deposition and the other for cooling, with their respective temperatures displayed.

4.5.5 Heat input

The heat input should replicate the heat input of a real industrial deposition. For low-fidelity cases, the peak temperatures will be around 1500-1700 degrees Celsius and the cooling temperatures will be around 100 degrees.

4.5.6 Dwell time

Dwell time is used for every case to mitigate the distortions further, and also to get realistic behavior and values from the process. Sufficient results to minimize distortions were found

to be around 10 seconds of dwell time or re-coating time [18]. This dwell time will be used to avoid large temperatures and distortions.

4.6 Error estimation

Utilizing global-error estimators facilitates the differentiation of distortions. L2-norm and L-infinity are two prevalent norms used for error estimation and controlling magnitudes in general. For example, it was found in [17] that the compensated part, by changing the mesh of a component during an AM process, has reduced to less than 50% of the original distortions, by changing the mesh. Whereas the indicator for assessing the results were by using the maximum L2-norm at local points. However, this does not provide a sufficient indicator for the error-estimation issue, as the average of the normal can be significantly higher. Also, because the volumes and domain can differ between the nominal scanning strategy and the modified one, due to different amount of activated elements.

Therefore, the solution implemented, and closer to indicating the error of the physical problem will be an average Euclidean norm, and maximum Euclidean norm will also be considered. Whereas, the average Euclidean norm is accordingly:

$$|u_{\text{average}}| = \frac{\sum_{\text{i}=0}^{n-1} \sqrt{u_{\text{x,i}}^2 + u_{\text{y,i}}^2 + u_{\text{z,i}}^2}}{n} \tag{42}$$

where, n denotes the number of points.

However, comparing the results when the number of elements differs, which will be the case when running a slightly different GCode, is relatively arduous. Since the mapping between the meshes is not one-to-one, it must therefore be between the closest nodes, point by point. Consequently, the results are not entirely accurate; even without AMR, the mesh between the two distinct codes should be very similar, but not completely identical. While multiple solutions were evaluated, by for example projecting the compensated mesh onto the original mesh in the post-processor *Paraview*. Therefore, a Python code was developed to address this issue.

4.7 Relaxation method

Compensating the mesh or GCode from an elasto-plastic analysis is challenging since the analysis is non-linear. To avoid overcompensating, a relaxation method will be utilized. This is based on employing a value less than the displacement scalars' upper bound. In this case, the scalars $\overline{u}_{\text{x}}$ and $\overline{u}_{\text{y}}$, from the displacement field used in the Python algorithm. This procedure will be repeated until a satisfactory outcome is achieved.

The influence coefficient, α, has to be introduced to systematically relax the system of equations, by modifying *Equation 41*.

$$\begin{aligned} X_{\text{n}} &= X_{\text{n}-1} - \alpha \cdot \overline{u}_{\text{x}} \\ Y_{\text{n}} &= Y_{\text{n}-1} - \alpha \cdot \overline{u}_{\text{y}} \end{aligned} \tag{43}$$

where n and $n-1$ refers to the current iteration and the past iteration, respectively. Thus, the method is done in an iterative process and continued until an adequate solution is found, $P_{\text{n}} \sim P_0$. Where P is the coordinate in the three-dimensional Euclidean space, $\mathbb{R}^3$.

Using the influence coefficient, a Python function was developed to simulate the compensation portion. Where the function accepts a dictionary of GCode coordinates with identical

keys for the node and displacement dictionaries and then modifies the GCode coordinates by inverting the displacement given.

```
def create_compensated_lists(X_coordinate, average_displacement_X,
↪  Y_coordinate, average_displacement_Y, influence_coefficient):
    # create a new list CompensatedX with values from X_coordinate,
    ↪  where the values have been subtracted by the corresponding value
    ↪  in average_displacement_X  multiplied by the influence
    ↪  coeffient.
    CompensatedX = [x - average_displacement_X[i]*influence_coefficient
    ↪  for i, x in enumerate(X_coordinate)]
    # create a new list CompensatedY with values from Y_coordinate,
    ↪  where the values have been subtracted by the corresponding value
    ↪  in average_displacement_Y multiplied by the influence coeffient
    ↪  .
    CompensatedY = [y - average_displacement_Y[i]*influence_coefficient
    ↪  for i, y in enumerate(Y_coordinate)]
    # return the new compensated lists CompensatedX and CompensatedY
    return CompensatedX, CompensatedY
```

5 Results

5.1 Temperatures

During the printing phase of the layer-by-layer printing strategy, the peak temperatures at each layer should be between 1500 and 1700 degrees Celsius. During the re-coating phase, these temperatures should drop to a few hundred degrees. As shown in *Figure 23*, these temperatures are not only necessary to achieve the desired behavior of the alloy, but also, to produce a solution that closely resembles actual AM process via LPBF.

Figure 25 depicts the temperatures during printing and cooling processes. Notably, the average temperature of the body of the compressor is substantially higher than that of its wings, as the body requires more time to cool than the less rigid components. This is because the body of the compressor is more thermally conductive and has a higher heat capacity than the wings, allowing it to retain more heat, requiring more time to cool.

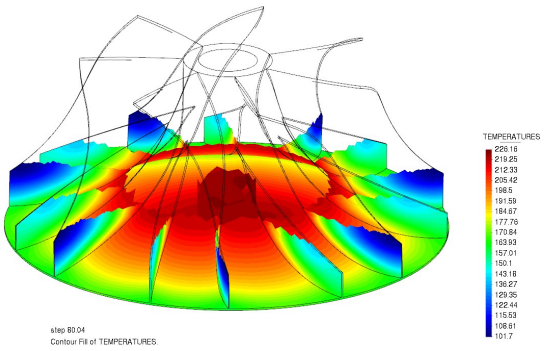

(a) Cooling temperatures during a re-coating (cooling) phase

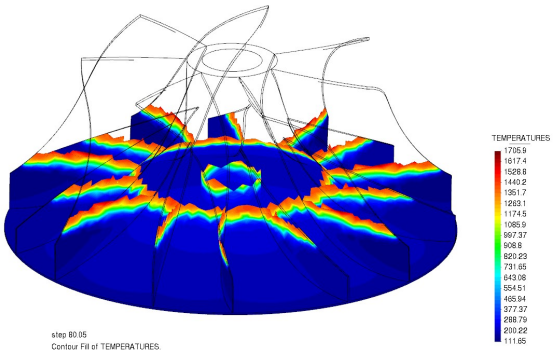

(b) Peak temperatures during a printing stage

Figure 25: Temperature field during cooling and printing for a layer-by-layer printing strategy

5.2 Numerical distortion-compensation of an impeller

5.2.1 Large impeller

First, the impeller was computed with only a thermal-elastic approach in order to assess the geometric compensation algorithm on simpler simulations before using a non-linear analysis. Compensating the entire GCode is not necessary for this component, since the rigid body is more prone to gravitational displacements, rather than tangential. Hence, the impeller is compensated "locally", whereas only the wings are compensated.

After a thermo elastic simulation *Figure 26* shows the contours of displacements where the distortions are close to null, after modifying the discrete nodal coordinates provided by the GCode at the wings of the impeller. Thereafter, the usage of a inviscid thermo-elastic model can be considered as a good model to get accurate results. However, in what follows, a visco-plastic-elasto-plastic model is considered.

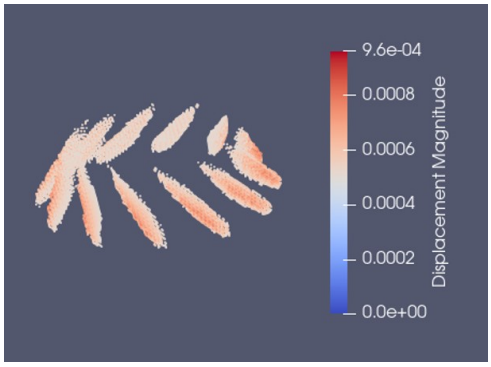

(a) Distortions from the nominal geometry of the impeller [mm]

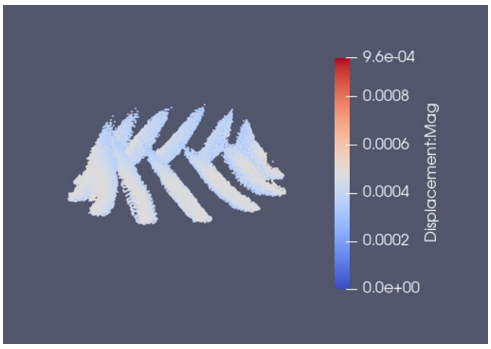

(b) Distortions from modifying the wings of the impeller [mm]

Figure 26: Comparison between distortions from the nominal geometry and distortions after modifying the geometry with the algorithm [mm] (thermal-elastic model)

A simulation of elasto-plastic behavior for the impeller is complex in term of non-linear behaviour. Depending on the discretization, the total amount of DOFs could be considerably larger, and in some cases, due to localized problems, the robustness of the approach is affected. However, similar to the elastic solution, the wings will only be compensated with a threshold and relaxation in order to avoid convergence issues.

With the elasto-plastic model, the displacement based on the unmodified (original) scanning strategy has larger displacements compared to the thermal-elastic simulations, and as before, the wings suffer the largest distortions as expected. Also, here an influence coefficient were used in an iterative manner to acquire a content solution. *Figure 27* shows the distortions from utilizing the unmodified scanning strategy. while *Figure 28* illustrates the results of the geometric compensation algorithm with a threshold that only considers the wings.

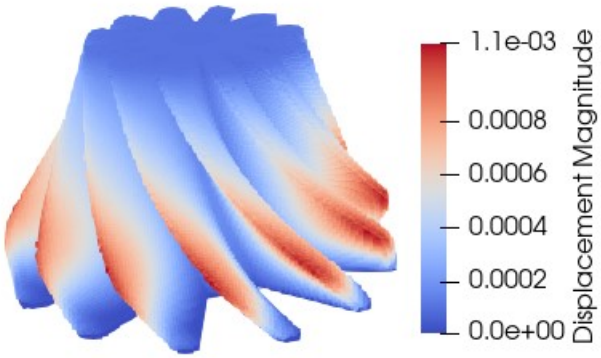

Figure 27: Original Euclidean norm for the impeller [mm]

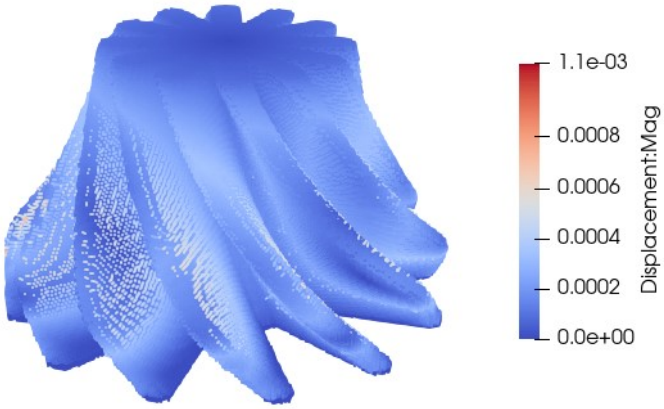

Figure 28: Euclidean norm for the impeller after modifying the original GCode [mm]

This resulted in an average of 40% lower distortions when comparing the average Euclidean norms, for the whole component, and 36% lower compared to the maximum Euclidean norm.

5.2.2 Small impeller

Mesh modification showed great results, whereas, the average Euclidean norm was 95% lower compared to the nominal geometry. *Figure 29a* illustrates the displacement magnitude for the nominal geometry. As the color scheme illustrates, *Figure 29b* shows almost null distortions, except for a few points at the wings that had smaller distortions from the nominal geometry.

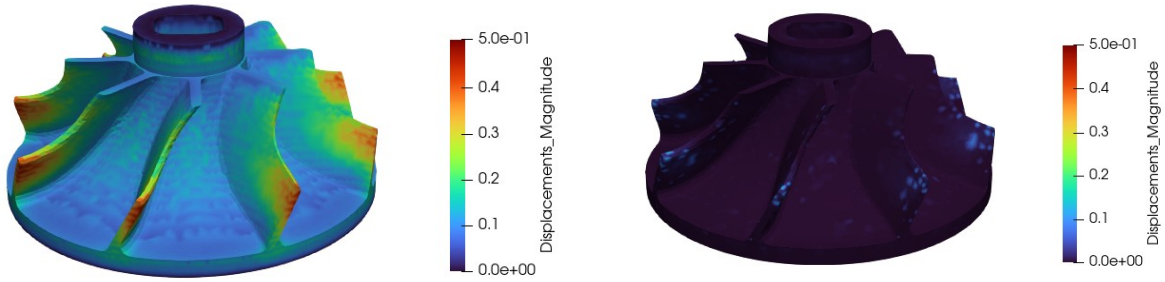

(a) Results from nominal geometry calculating with a triangular mesh without a GCode [m]

(b) Results from modifying the mesh of the small impeller [m]

Figure 29: Comparison between distortions from the nominal geometry and distortions after modifying the geometry by mesh modification

However, *Figure 29b* does not depict the entire methodology; the component is fully simulated numerically, but a GCode must be generated from the modified STL file in order to determine the correct results

The mesh compensation yields excellent results, when only comparing the meshes. This is illustrated in*Figure 30*. The final results are shown in *Figure 30b*, which shows that the average Euclidean norm were reduced by nearly 50%, and maximum displacement magnitude reduced by nearly 50%. as well. In this experiment the component was

generated by creating a GCode from the compensated geometry from the mesh with null distortion, see *Figure 29b*.

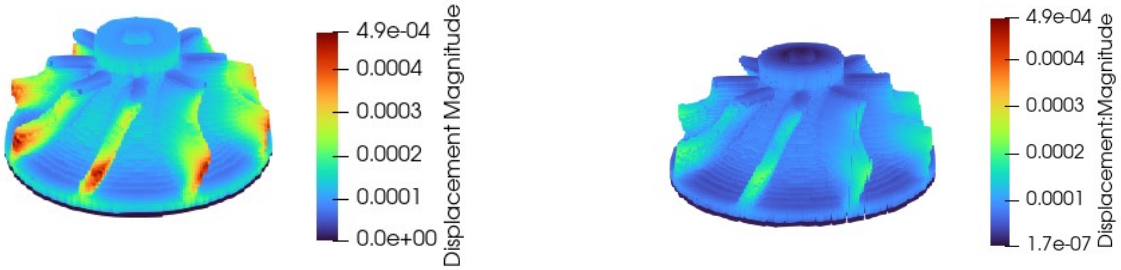

(a) Results from nominal geometry and GCode [m]

(b) Results from creating a new GCode from the warped STL file [m]

Figure 30: Comparison between distortions from the nominal geometry and distortions after modifying the geometry by mesh modification [m]

However, modifying the GCode with the algorithm causes around 30% fewer average global distortions, while for the maximum it reduces with nearly 36%. Similar to the results achieved by the larger impeller.

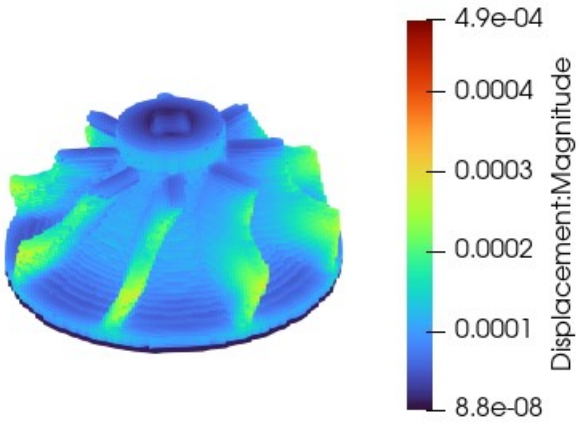

Figure 31: Results from modifying the GCode with the algorithm [m]

5.3 Numerical distortion-compensation of a gear

The original scanning strategy used for the gear showed large displacements at the outer rim of the gear, see *Figure 32*, outside the large volumetric body. With large tangential displacements, the threshold used will be only the part with these displacements, and the large volumetric body with mostly distortions due to gravitational forces will be left out.

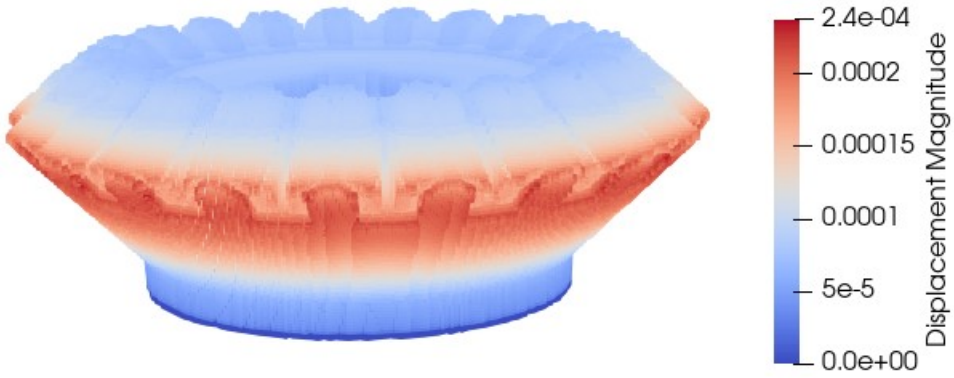

Figure 32: Results from nominal GCode [mm]

Figure 33 depicts the distortions after the geometric compensation process. The average Euclidean norm decreased by 31%, and the maximum displacement magnitude decreased by nearly 35%.

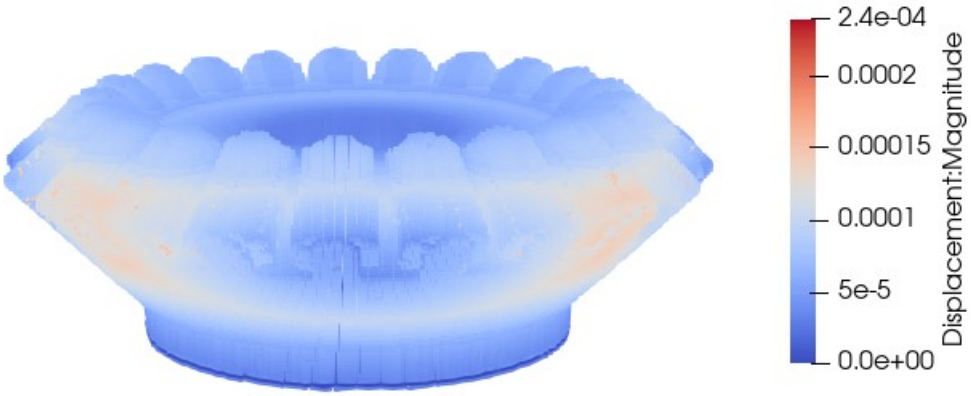

Figure 33: Results from modifying the GCode [mm]

The results, by using the geometric compensation algorithm, again showed satisfactory results of decreasing the distortions. However, the outer part of the gear, after compensation, has an inconsistent compensation. There are some parts of the outer rim that has a larger displacement, even with the symmetrical geometry of the gear.

5.4 Numerical distortion-compensation of a compressor

Compared to the previous experiments, the geometry of the compressor is the most complex, with curved wings at the top and an inclined cylindrical geometry. Due to bending and the low rigidity of the walls, the wings will experience significant deformations. *Figure 34* illustrates the results from simulating the original CAD file. In this instance, the computation time required to generate a smooth mesh was significant. The algorithm will thus utilize the displacement field from the mesh, as shown in *Figure 34*.

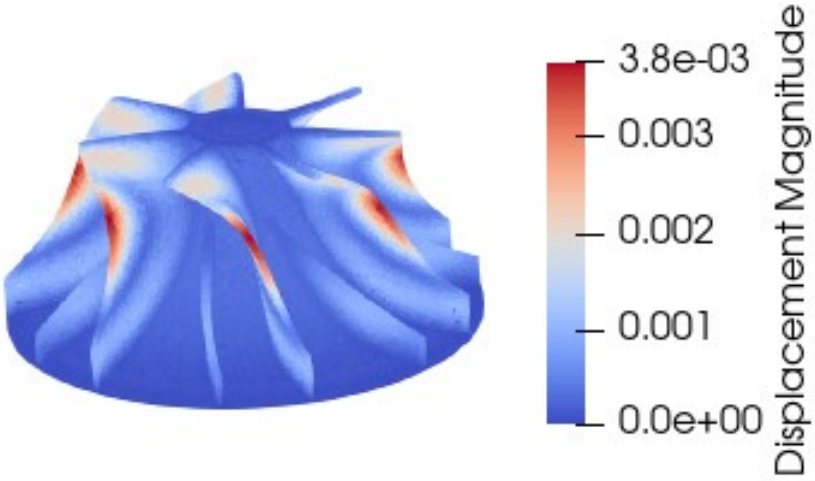

Figure 34: Displacement field from original geometry [m]

Both strategies will be used to compare the algorithm's precision. The results of compensating the original GCode for the compressor with the displacement field generated by automatic mesh generation are shown in *Figure 35b*. The precision of the *Figure 35b* is relatively poor, with many points "overcompensated" and some areas "undercompensated", such as at the bottom of the wings.

Observe that there is no difference between using a displacement field from the manual mesh generation or the automatic mesh generation, when comparing average euclidean norm.

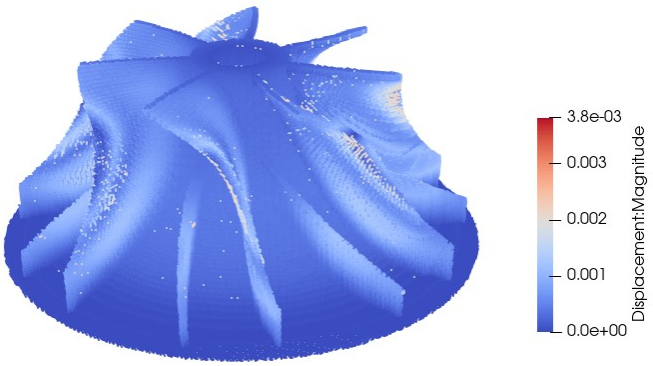

(a) Results from modifying the GCode with displacement field from manual mesh generation [m]

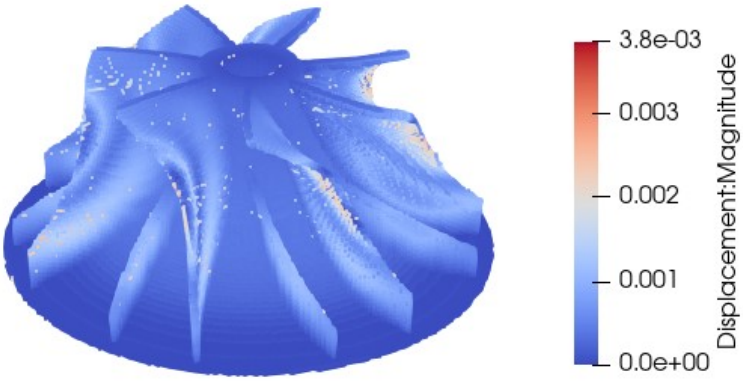

(b) Results from modifying the GCode with displacement field from automatic mesh generation [m]

Figure 35: Comparison between modified geometry from the displacement field from the automatic mesh generation and displacement field from the simulation done with the triangular mesh model

6 Discussion

First, there were some convergence issues, with the impeller, in the initial simulations. The issue was floating elements, particularly for plastic analysis; deactivating floating elements resolved this issue. However, this will result in a slight increase in computational time.

The impeller's wings exhibited the greatest distortions. This is likely due to the fact that the wings are less rigid than the rest of the impeller. Since the impeller is composed of a large, extremely rigid body, it can withstand large temperature gradients without exceeding its yield strength. However, for the less rigid component, this will result in stresses that exceed the titanium's yield strength. In addition, the Z-displacement is disproportionately large, at least at the wings, which contributes significantly to the overall warpage. Since the layer-by-layer strategy has been used, the Z-coordinates hinder the effectiveness of the modifying strategy.

Moreover, if the substrate is not taken into account during the fabrication process, thermal differences between the substrate and the deposited layer will significantly contribute to the distortions. In addition, due to thermal losses caused by convection in the substrate, it may take time for the substrate's average temperature to approach that of the constructed component. Consequently, both the dynamic thermal differences and the distortions are drastically reduced. Being less severe if the substrate is ignored. Since the purpose of the study was to assess the precision of the geometric distortion algorithm, this was omitted and should not have affected the method's precision.

Moreover, the algorithm requires a relatively fine mesh in comparison to the increment of the code. Not only due to the algorithm, but also due to the accuracy of the numerical analysis. However, the algorithm demonstrated promise when applied to displacement fields from multiple sources, making it applicable to experimental data. Therefore, the component can be manufactured in a laboratory, and the displacement can be scanned and used to modify the GCode in the future.

Modifying the mesh has great results, providing a solution that is fully compensated. However, the mesh does not yield a fully compensated result when generating an STL file and GCode for manufacturing. Theoretically, the solution should never be reach zero distortions because Z-distortions are not considered in LPBF processes. It is essential that the Z-direction geometry of each layer is consistent, meaning that the height should not be altered. If the height is altered, it is possible that the recoating machinery will be damaged when recoating powder from a previous step whose modification was insufficient. It is not possible with the current LPBF method.

Also, the GCode has a low level of discretization, and the method for modifying it can be laborious. For example, If the GCode is based solely on a single linear printing command, which is neither an industrial component nor a scenario that would be considered in an LPBF process, it would be illogical to modify two coordinates when the mesh and distortion can be substantial; depending on the refinement level.

According to the author's knowledge, comparing components with different mesh sizes may give faulty results, and the comparison was done by calculating the distance between every point. Also, modifying the GCode may result in the activation of elements that are not in line with the original mesh generation based on the nominal geometry. Consequently, the nodes will move in accordance with the element size, and the measurement will produce nodes that appear to be overcompensated but may not be. A possible solution would be to reduce the size of the melt-pool, thereby preventing the activation of elements that are

far from their nominal geometry. However, for accurate determination, it must be printed in the laboratory.

Also, the precision of the GCode commands themselves are uncertain, as modifying the GCode by the algorithm may be insufficient to take into account of the size of the heat input. Meaning, compensating a coordinate with an extremely low displacement might not change anything. Since the size of the laser can be larger than the compensation.

7 Conclusions

There were several achievements with the thesis. First, the results of the algorithm were sufficient, the reduction in global average Euclidean norm was around 30% for all the cases, 40% for the large impeller. Thus, the algorithm is a robust method to compensate for distortions in AM processes. However, compared to modifying the mesh and creating a new STL file, a new GCode proved to have greater results, with a reduction of 50%. *Table 5* summarizes the final results for all the cases, and their respective method, the reduction of the average Euclidean norm.

Table 5: Comparison of the global average distortion

Case	Reduction of average distortion
Large impeller (algorithm)	40%
Small impeller (mesh modification)	50%
Small impeller (algorithm)	30%
Gear (algorithm)	31%
Compressor (algorithm)	28%

Also, the algorithm's precision and sufficiency were examined. It was determined that the algorithm's precision did not vary depending on where from the displacement field was obtained.

In addition to, including the sufficiency of the relaxation technique and the problems with floating elements. The following conclusions were drawn from this thesis:

- Changing the mesh yields a partially compensated solution.
- Satisfactory results has been obtained when modifying the GCode. However, the accuracy is insufficient.
- Floating elements are an issue when generating meshes automatically using modified GCodes.
- The relaxation technique is effective for non-linear simulations.
- The GCode compensating algorithm is practical and could be used with data from any displacement field (experimental or numerical).

7.1 Future research

Since the GCode algorithm uses a displacement field, the displacement field from experimental data might be more useful. The precision and mapping between the GCode commands and displacement from real manufacturing components might have greater precision than, for example, an automatic mesh generation or a smooth triangular mesh.

Another interesting future development is the usage of a method of 3D scanning for the component after manufacturing, and with the distortions obtained create a surface mesh and an STL file. Thereafter, create a mathematical model that can identify the GCode command that was "related" to the distorted node, since it might not be the closest distance. Subsequently, the compensation algorithm can be utilized.

References

[1] Indradev Samajdar Bert Verlinden Julian Driver and Roger D. Doherty. *Thermo-mechanical Processing of Metallic Materials*. Elsevier Ltd, 2007.

[2] Michael Gouge and Pan Michaleris. *Thermo-Mechanical Modeling of Additive Manufacturing*. Butterworth-Heinemann, 2018.

[3] *Powder Bed Fusion What is Powder Bed Fusion?* https://engineeringproductdesign.com/knowledge-base/powder-bed-fusion/. Accessed: 2022-11-15.

[4] Erik R Denlinger, Jarred C Heigel and Panagiotis Michaleris. 'Residual stress and distortion modeling of electron beam direct manufacturing Ti-6Al-4V'. In: *Proceedings of the Institution of Mechanical Engineers, Part B: Journal of Engineering Manufacture* 229.10 (2015), pp. 1803–1813. DOI: 10.1177/0954405414539494.

[5] Bhaskar Dutta and Francis H. Froes. *Additive Manufacturing of Titanium Alloys-State of the Art, Challenges, and Opportunities*. Butterworth-Heinemann, 2016.

[6] Bhaskar Dutta. 'Directed Energy Deposition (DED) Technology'. In: *Encyclopedia of Materials: Metals and Alloys*. Ed. by Francisca G. Caballero. Oxford: Elsevier, 2022, pp. 66–84. ISBN: 978-0-12-819733-2. DOI: https://doi.org/10.1016/B978-0-12-819726-4.00035-1. URL: https://www.sciencedirect.com/science/article/pii/B9780128197264000351.

[7] Zhihua Tian et al. 'A Review on Laser Powder Bed Fusion of Inconel 625 Nickel-Based Alloy'. In: *Applied Sciences* 10.1 (2020). ISSN: 2076-3417. URL: https://www.mdpi.com/2076-3417/10/1/81.

[8] Andrew C. Brown and Deon de Beer. 'Development of a stereolithography (STL) slicing and G-code generation algorithm for an entry level 3-D printer'. In: (2013), pp. 1–5. DOI: 10.1109/AFRCON.2013.6757836.

[9] Carlos Augusto Moreira Filho. 'Finite element simulation of additive manufacturing with enhanced accuracy'. In: (July 2022), pp. 1–199. DOI: https://upcommons.upc.edu/handle/2117/371627.

[10] Iñaki Setien et al. 'Empirical methodology to determine inherent strains in additive manufacturing'. In: *Computers and Mathematics with Applications* 78.7 (2019). Simulation for Additive Manufacturing, pp. 2282–2295. ISSN: 0898-1221. DOI: https://doi.org/10.1016/j.camwa.2018.05.015. URL: https://www.sciencedirect.com/science/article/pii/S0898122118302839.

[11] Shukri Afazov et al. 'An improved distortion compensation approach for additive manufacturing using optically scanned data'. In: *Virtual and Physical Prototyping* 16.1 (2021), pp. 1–13.

[12] Xufei Lu et al. 'Substrate design to minimize residual stresses in Directed Energy Deposition AM processes'. In: *Materials & Design* 202 (2021), p. 109525. ISSN: 0264-1275. DOI: https://doi.org/10.1016/j.matdes.2021.109525. URL: https://www.sciencedirect.com/science/article/pii/S0264127521000782.

[13] Konstantin Babkin et al. 'Distortion prediction and compensation in direct laser deposition of large axisymmetric Ti-6Al-4V part'. In: *Procedia CIRP* 94 (2020). 11th CIRP Conference on Photonic Technologies [LANE 2020], pp. 357–361. ISSN: 2212-8271. DOI: https://doi.org/10.1016/j.procir.2020.09.145. URL: https://www.sciencedirect.com/science/article/pii/S2212827120313330.

[14] Shukri Afazov et al. 'Distortion prediction and compensation in selective laser melting'. In: *Additive Manufacturing* 17 (2017), pp. 15–22. ISSN: 2214-8604. DOI: https://doi.org/10.1016/j.addma.2017.07.005. URL: https://www.sciencedirect.com/science/article/pii/S2214860416303104.

[15] Shukri Afazov et al. 'A methodology for precision additive manufacturing through compensation'. In: *Precision Engineering* 50 (2017), pp. 269–274. ISSN: 0141-6359. DOI: https://doi.org/10.1016/j.precisioneng.2017.05.014. URL: https://www.sciencedirect.com/science/article/pii/S0141635917301484.

[16] Max Biegler et al. 'Geometric distortion-compensation via transient numerical simulation for directed energy deposition additive manufacturing'. In: *Science and Technology of Welding and Joining* 25.6 (2020), pp. 468–475. DOI: 10.1080/13621718.2020.1743927.

[17] Anas Yaghi et al. 'Design against distortion for additive manufacturing'. In: *Additive Manufacturing* 27 (2019), pp. 224–235. ISSN: 2214-8604. DOI: https://doi.org/10.1016/j.addma.2019.03.010. URL: https://www.sciencedirect.com/science/article/pii/S2214860418308583.

[18] Erik R. Denlinger et al. 'Effect of inter-layer dwell time on distortion and residual stress in additive manufacturing of titanium and nickel alloys'. In: *Journal of Materials Processing Technology* 215 (2015), pp. 123–131. ISSN: 0924-0136. DOI: https://doi.org/10.1016/j.jmatprotec.2014.07.030. URL: https://www.sciencedirect.com/science/article/pii/S0924013614002891.

[19] Christoph Schmutzler et al. 'Pre-compensation of Warpage for Additive Manufacturing'. In: *Journal of Mechanics Engineering and Automation* 6 (Aug. 2016). DOI: 10.17265/2159-5275/2016.08.002.

[20] Christoph Schmutzler et al. 'Pre-compensation of Warpage for Additive Manufacturing'. In: *Institute for Machine Tools and Industrial Management, Technical University Munich* Augsburg 86153 (2019).

[21] Christoph Schmutzler, Alexander Zimmermann and Michael F. Zaeh. 'Compensating Warpage of 3D Printed Parts Using Free-form Deformation'. In: *Procedia CIRP* 41 (2016). Research and Innovation in Manufacturing: Key Enabling Technologies for the Factories of the Future - Proceedings of the 48th CIRP Conference on Manufacturing Systems, pp. 1017–1022. ISSN: 2212-8271. DOI: https://doi.org/10.1016/j.procir.2015.12.078. URL: https://www.sciencedirect.com/science/article/pii/S2212827115011579.

[22] Christian Eschey, Stefan Feldmann and Michael Zäh. 'Rule-Based Free-Form Deformation for Additive Layer Manufacturing'. In: Aug. 2011, pp. 363–374.

[23] Jun Cao, Michael A. Gharghouri and Philip Nash. 'Finite-element analysis and experimental validation of thermal residual stress and distortion in electron beam additive manufactured Ti-6Al-4V build plates'. In: *Journal of Materials Processing Technology* 237 (2016), pp. 409–419. ISSN: 0924-0136. DOI: https://doi.org/10.1016/j.jmatprotec.2016.06.032. URL: https://www.sciencedirect.com/science/article/pii/S0924013616302126.

[24] Erik R. Denlinger. 'Thermo-Mechanical Modeling of Additive Manufacturing'. In: Butterworth-Heinemann, 2018, pp. 183–195. ISBN: 978-0-12-811820-7. DOI: https://doi.org/10.1016/B978-0-12-811820-7.00013-6. URL: https://www.sciencedirect.com/science/article/pii/B9780128118207000136.

[25] Qianru Wu et al. 'Residual stresses and distortion in the patterned printing of titanium and nickel alloys'. In: *Additive Manufacturing* 29 (2019), p. 100808. ISSN: 2214-8604. DOI: https://doi.org/10.1016/j.addma.2019.100808. URL: https://www.sciencedirect.com/science/article/pii/S2214860419307663.

[26] J. DANTZIG P. MICHALERIS and D. TORTORELLI. 'Minimization of Welding Residual Stress and Distortion in Large Structures'. In: *WELDING JOURNAL* 41 (1999), pp. 361–365.

[27] M. V. Deo. 'Minimization of bowing distortion in welded stiffeners using differential heating'. In: *WELDING JOURNAL* 41 (1999), pp. 78–98.

[28] J. LI. 'Minimizing buckling distortion in welding by weld cooling'. In: *WELDING JOURNAL* 41 (1999), pp. 214–240.

[29] R. P. MARTUKANITZ S. M. KELLY and E. W. REUTZEL. 'Minimizing buckling distortion in welding by hybrid laser-arc welding'. In: *WELDING JOURNAL* 41 (1999), pp. 241–272.

[30] M. Chiumenti et al. 'Numerical modeling of the electron beam welding and its experimental validation'. In: *Finite Elements in Analysis and Design* 121 (2016), pp. 118–133. ISSN: 0168-874X. DOI: https://doi.org/10.1016/j.finel.2016.07.003. URL: https://www.sciencedirect.com/science/article/pii/S0168874X16301378.

Appendix

```python
def classify_points(displacement_mapping, threshold):
    """
    This function classifies the points in the displacement_mapping
    ↪ dictionary as either dangerous or safe
    based on the norm of the displacement.

    Parameters:
    displacement_mapping (dict): a dictionary that maps each point to
    ↪ its displacement
    threshold (float): the threshold value used to determine whether a
    ↪ point is dangerous or safe

    Returns:
    tuple: a tuple containing two lists, one containing the dangerous
    ↪ points and one containing the safe points
    """
    dangerous_points = [(point, displacement) for point, displacement in
    ↪  displacement_mapping.items() if displacement[3] > threshold]
    safe_points = [(point, displacement) for point, displacement in
    ↪  displacement_mapping.items() if displacement[3] <= threshold]
    return dangerous_points, safe_points

def getClosestGcodePoint(meshPoint, gcodePoints):
    """
    Given a mesh point and a list of gcode points, finds the closest
    ↪ gcode point to the mesh point
    by calculating the euclidean distance between the mesh point and
    ↪ each point in gcodePoints.
    """
    # Use numpy to calculate euclidean distance between meshPoint and
    ↪  each point in gcodePoints
    distances = np.linalg.norm(gcodePoints - meshPoint, axis=1)
    # Find the index of the closest point in gcodePoints
    idxClosest = np.argmin(distances)
    # Return the closest point and its index in gcodePoints
    return gcodePoints[idxClosest], idxClosest

def find_closest_points(reference_nodes, target_points):
    """
    Given a list of reference_nodes and a list of target_points, finds
    ↪ the closest point from target_points for each reference_node.
    Returns a dictionary where key is the reference_node and the value
    ↪ is a tuple of closest point and its index in target_points
    """
    result = []
```

```
    closest_indices = []
    for i in range(len(reference_nodes)):
        closest_point, closest_index =
        ↪ getClosestGcodePoint(reference_nodes[i], target_points)
        result.append(closest_point)
        closest_indices.append(closest_index)
    return result, closest_indices


def map_dangerous_points(key_list, x_displacement, y_displacement):
    # Initialize two empty dictionaries to store x and y displacement
    ↪ respectively
    x_displacement_dict = {}
    y_displacement_dict = {}
    # Iterate over the key, x displacement and y displacement using the
    ↪ zip function
    for key, x_disp, y_disp in zip(key_list, x_displacement,
    ↪ y_displacement):
        #Assign the key and its corresponding x displacement to
        ↪ x_displacement_dict
        x_displacement_dict[key] = x_disp
        #Assign the key and its corresponding y displacement to
        ↪ y_displacement_dict
        y_displacement_dict[key] = y_disp
    #Return the two dictionaries
    return x_displacement_dict, y_displacement_dict


def create_compensated_lists(X_coordinate, average_displacement_X,
↪ Y_coordinate, average_displacement_Y, influence_coefficient):
    # create a new list CompensatedX with values from X_coordinate,
    ↪ where the values have been subtracted by the corresponding value
    ↪ in average_displacement_X  multiplied by the influence
    ↪ coeffient.
    CompensatedX = [x - average_displacement_X[i]*influence_coefficient
    ↪ for i, x in enumerate(X_coordinate)]
    # create a new list CompensatedY with values from Y_coordinate,
    ↪ where the values have been subtracted by the corresponding value
    ↪ in average_displacement_Y multiplied by the influence coeffient
    ↪ .
    CompensatedY = [y - average_displacement_Y[i]*influence_coefficient
    ↪ for i, y in enumerate(Y_coordinate)]
    # return the new compensated lists CompensatedX and CompensatedY
    return CompensatedX, CompensatedY
```